Bioorthogonal tools to study fatty acid uptake in immune cells

Bertheussen, K.

Citation

Bertheussen, K. (2026, January 13). *Bioorthogonal tools to study fatty acid uptake in immune cells*. Retrieved from https://hdl.handle.net/1887/4286403

4

Phenotypic and Multiomic Differences Between T cells with a Differential Sterculic Acid Uptake

Abstract

T cells undergo rapid metabolic reprogramming during activation to support the high energy demands of cell growth and proliferation. This metabolic shift is supported by the uptake of exogenous nutrients from the cells' environment. For certain nutrients, such as glutamine and glucose, the uptake mechanisms and biological effects of high or low uptake are well understood. This is less the case for fatty acids, where neither the uptake mechanism nor the precise biological effects of uptake have been characterized. Here this problem is addressed using bioorthogonal chemistry: by exposing splenocytes to sterculic acid, a bioorthogonal analogue of oleic acid, followed by fluorescent-activated cell sorting, a method was developed to multiplex nutrient uptake with phenotypic, proteomic, and transcriptomic differences on a single-cell level. Cells with a high uptake of exogenous sterculic acid took on a more effector-like phenotype and metabolism compared to low-uptake cells. Additionally, these cells upregulated the expression of key genes and proteins related to glucose metabolism, fatty acid synthesis, and the mevalonate pathway, also indicating a more effector-like state. These effects became more pronounced if the T cells were activated *in vitro* with αCD3/αCD28 antibodies prior to sterculic acid uptake.

Introduction

Upon activation, T cells undergo a rapid metabolic reprogramming to support their increased cell growth and proliferation. During the activation process, quiescent T cells, which mainly rely on catabolic metabolism and oxidative phosphorylation (OXPHOS) for their energy supply, shift their metabolism towards aerobic glycolysis and anabolism to support their high energetic and biosynthetic demands.[1–3]

Interestingly, this metabolic shift is heavily supported by an increased uptake of exogenous nutrients such as glucose and amino acids.[4,5] The uptake of exogenous free fatty acids (FFAs) are known to be essential for the activation and survival of several T cell subsets.[6,7] While fatty acids (FAs) in quiescent T cells are prone to degradation via fatty acid oxidation (FAO) to fuel ATP production via OXPHOS, T cells upregulate *de novo* fatty acid synthesis and fatty acid uptake upon activation.[6] Furthermore, activated T cells are known to upregulate other lipid biosynthetic pathways such as cholesterol biosynthesis, to support their increased need for membrane components.[8] A more detailed description of the metabolic reprogramming of T cells upon activation can be found in Chapter 1.

Previous work has shown that the exposure of T cells to oleic acid (OA) affects their survival, proliferation, activation, and differentiation.[9–15] However, since the use of the native form of OA in these experiments does not allow for the detection of intracellular OA, limited information about the actual cellular OA uptake on a single-cell level could be gathered. Additionally, it could not be determined if the observed effects were a result of extracellular exposure of OA in the culture medium, or cellular uptake of OA.

This thesis has demonstrated the effective manner by which the bioorthogonal OA analogue, sterculic acid (StA), can be used to study fatty acid uptake in cells. In this Chapter, the uptake of StA in primary cells isolated from mouse spleens was explored at a single-cell level. Murine splenocytes are a heterogenous population of immune cells, but contain a large portion of T cells (~30-35%).[16,17] It was therefore envisaged that the detection of StA, using the mild inverse electron-demand Diels-Alder (IEDDA) reaction, could be used to distinguish cells with a high and low FA uptake within the heterogenous splenocyte mixture. The focus was to identify factors governing the ability of a cell to take up FAs during activation. Differences between populations after short pulses of FA uptake, at times before or after activation, were deemed to be the most informative, rather than examining the phenotype of the cells long after immune activation to determine the functional effect of FA uptake on later phenotypes.

With these proof-of-principle experiments, the uptake of StA was monitored on a single-cell level by fluorescent detection with flow cytometry. Simultaneously, proteomic and transcriptomic differences between cells with differential StA uptake were explored. The transcriptomic differences were investigated using single-cell RNA sequencing (scRNAseq), to gain further insight into how the heterogeneous splenocyte population responded to the uptake of exogenous StA.

Results & Discussion

As a strategy to multiplex OA uptake with phenotypic and multiomic information, a workflow was developed where murine splenocytes were exposed to StA (Figure 1). In order to do this, the method described in Chapter 2 of this thesis was re-developed: Splenocytes – isolated from fresh mouse spleens by mechanical homogenization[18] – were incubated with a short pulse of StA (Figure 1A) and the cyclopropene group was used to perform an inverse electron-demand Diels-Alder (IEDDA) click reaction with fluorophore **7** (Figure 1B).

The cells were analysed by flow cytometry and a variation in fluorescent signal spanning one order of magnitude was observed in a single sample (Figure S1A), suggesting highly heterologous fatty acid uptake in this complex mixture of immune cells. In addition, the same experiment was performed after first activating the T cell population within the splenocytes. Incubation with αCD3/αCD28 antibodies[19] overnight, prior to lipid uptake analysis, would allow a comparative exploration of the fatty acid uptake in both naïve and activated T cells in comparison – all within the complex mixture of other immune cells of the spleen – to investigate potential differences in the response upon activation. Upon T cell activation with αCD3/αCD28, the variation in fluorescent signal during flow cytometry increased to almost two orders of magnitude (Figure S1B).

To determine whether any cell-type intrinsic factors were responsible for the differences in lipid uptake, the high and low uptake cells were isolated by fluorescence-activated cell sorting (FACS, Figure 1C). The fluorescence of **7** was used to separate the highest and lowest quartile of cells based on StA uptake for further analysis of their metabolism, transcriptomes, and proteomes (Figure 1D).

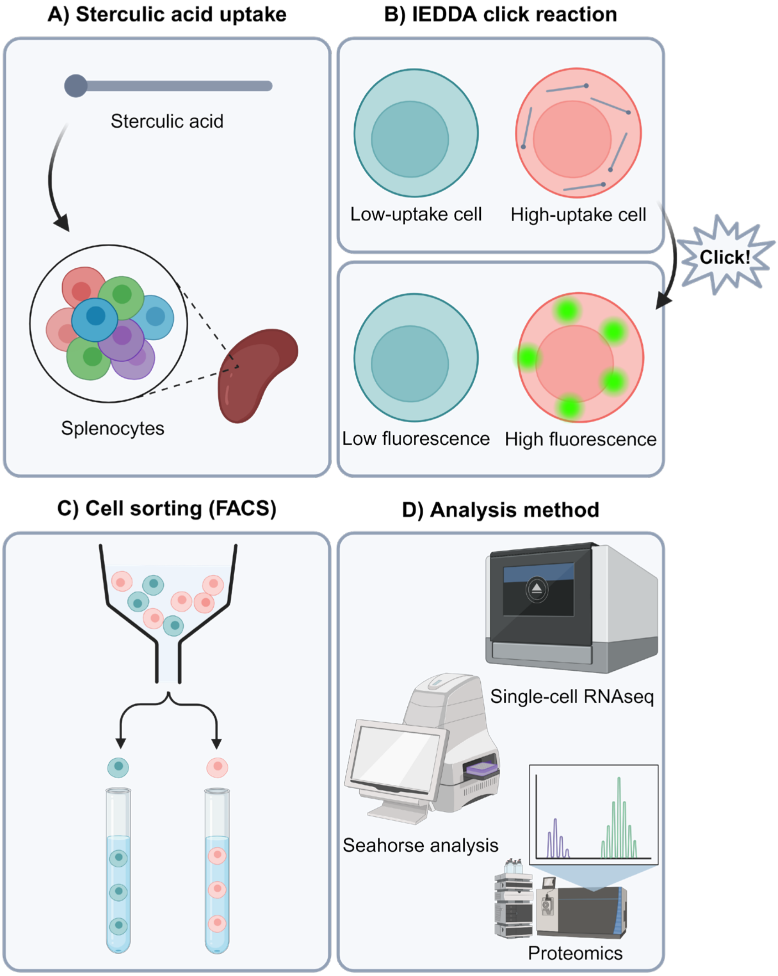

Figure 1: *Illustration showing an overview of the workflow from* ***A)*** *sterculic acid uptake in murine splenocytes,* ***B)*** *inverse electron-demand Diels-Alder (IEDDA) reaction,* ***C)*** *fluorescence-activated cell sorting (FACS), and* ***D)*** *the subsequent analysis methods. The figure is made with BioRender.*

Phenotypic differences between T cells with differential StA-uptake

To focus initially on a smaller subset of cells from the complex splenocyte mixture, the highest and lowest quartile of StA uptake in CD3+/CD4+ T cells were sorted by FACS according to the gating strategies shown in Figure S1. The well-known T cell activation markers CD44 and CD62L[20,21] were also included in the antibody panel.

Upon analysis of the cells with differential StA-uptake by flow cytometry, it was apparent that the size of the high-uptake cells was larger than the low-uptake cells, based on median forward scatter (FSC), for both naïve (Figures 2A & 2B) and activated (Figures 2C & 2D) CD3+/CD4+ T cells. The activated T cells also showed increased cellular granularity, as measured by median side scatter (SSC), upon high StA-uptake (Figures 2C & 2D). However, no difference in cellular granularity was observed for the naïve T cells (Figures 2A & 2B). Increased cell size and granularity is known to occur in T cells upon activation[22,23], and the increased cell size has (partially) been attributed to an increase in activity of mammalian target of rapamycin (mTOR), a key regulator of many facets of cellular metabolism.[24] Therefore, these results could indicate that the high-uptake T cells are in a more effector-like state than the low-uptake cells, and that the differentiation of these cells affect their ability to take up exogenous FAs.

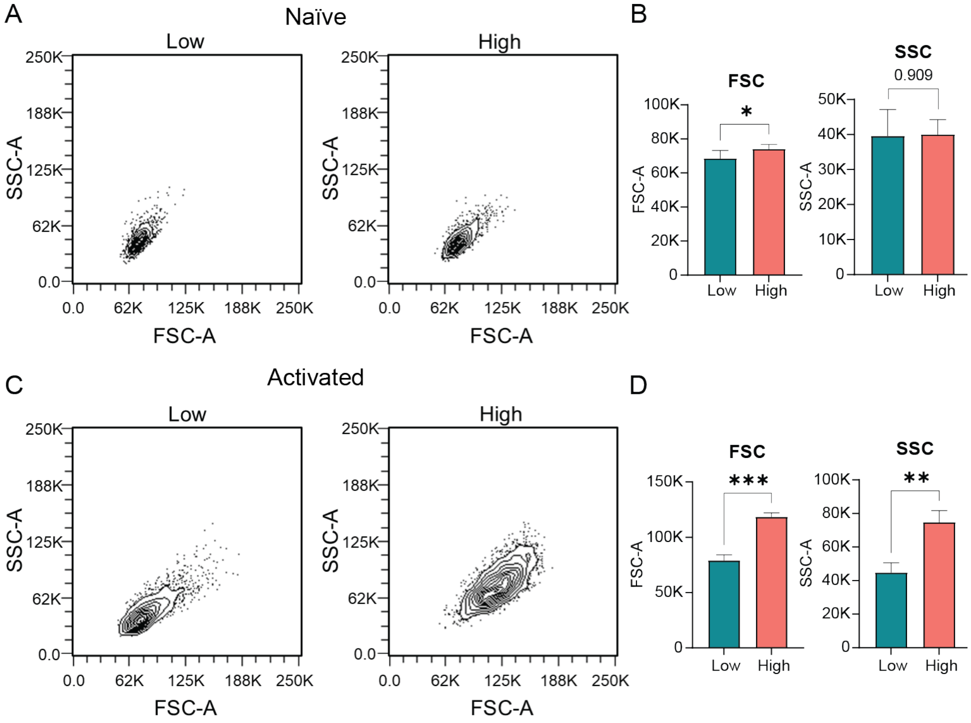

*__Figure 2:__ CD3+/CD4+ T cells with high StA-uptake are larger and more granulated than low-uptake cells, especially when activated. __A)__ Forward scatter (FSC) and side scatter (SSC) plots of the low- and high-uptake populations of naïve T cells, and subsequent __B)__ quantification of the median FSC and SSC (based on 5 biological replicates). __C)__ Forward scatter (FSC) and side scatter (SSC) plots of the low- and high-uptake populations of activated T cells, and subsequent __D)__ quantification of the median FSC and SSC (based on 3 biological replicates). Unpaired, two-way, student's T test. * = $P \leq 0.05$, ** = $P \leq 0.01$, *** = $P \leq 0.001$*

Upon further investigation of the FACS data it became clear that there was a shift in the expression of the CD44 and CD62L markers in the high-uptake population compared to the low-uptake population of naïve T cells, (Figure 3A). Upon quantification of the median fluorescence intensity (MFI), a trend of increased CD44 expression is observed, while CD62L expression was significantly decreased at the cell surface in the high-uptake population (Figure 3B). Again, this indicates that the cells in the high-uptake population are in a more activated state than the low-uptake population. For the activated T cells, all cells were activated by a αCD3/αCD28 antibody cocktail prior to StA uptake and FACS. Interestingly, a similar pattern was observed for the activated T cells where a trend towards increased expression of CD44 and decreased expression of CD62L at the cell surface was observed (Figures 3C & 3D). This suggests that the T cell population after *in vitro* activation is still a heterogeneous mixture of T cell subsets, and that the high StA-uptake population appears to be dominated by more effector-like T cells. This is in accordance with the previous observation of increased cell size (and granularity) of high-uptake T cells.

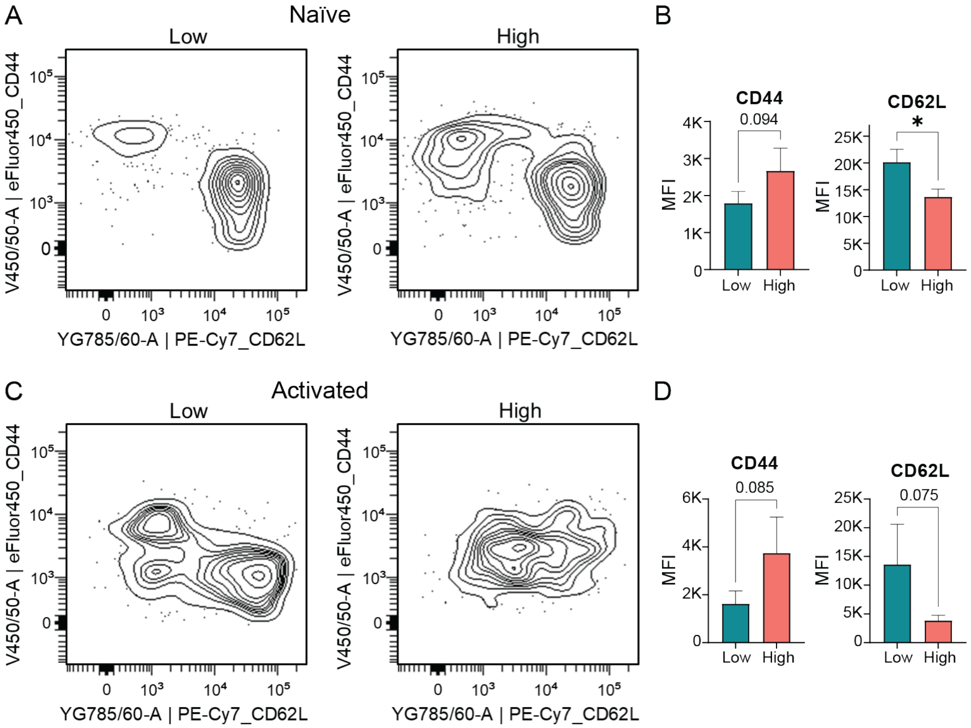

Figure 3: *CD3+/CD4+ T cells with a high StA-uptake show increased expression of CD44 and decreased expression of CD62L, compared to low-uptake cells, indicating T cell activation.* ***A)*** *Plots showing CD44 & CD62L expression of low- and high-uptake populations of naïve T cells, and subsequent* ***B)*** *quantification of median fluorescence intensity (MFI) of CD44 & CD62L expression (based on 3 biological replicates).* ***C)*** *Plots showing CD44 & CD62L expression of low- and high-uptake populations of activated T cells, and subsequent* ***D)*** *quantification of median fluorescence intensity (MFI) of CD44 & CD62L expression (based on 3 biological replicates). Unpaired, two-way, student's T test. * = P ≤ 0.05.*

Following cell sorting of CD3+/CD4+ T cells by FACS, the metabolic energetics of cells with low and high uptake of StA were also examined. The oxygen consumption rate (OCR) and extracellular acidification rate (ECAR) were measured using a Seahorse analyser[25], to assess changes in mitochondrial respiration and glycolysis, respectively. From these data, the percentage-wise reliance of these cells on oxidative phosphorylation (%OXPHOS) and glycolysis (%Glycolysis) were determined (Figure 4).

The metabolic energy map (Figure 4A) provides valuable insights into the metabolic phenotypes of both naïve and activated splenocytes and their T cell subsets. For naïve cells, both low- and high-uptake populations exhibit a quiescent metabolic phenotype. However, low-uptake cells appear more quiescent compared to their high-uptake counterparts. In contrast, the mixed, unsorted splenocyte population displays a more energetic phenotype, characterised by an overall higher metabolic capacity. Upon activation, the metabolic energy map reveals notable changes to the T cells energy profiles. Low-uptake T cells, while retaining a predominantly quiescent phenotype, show an increase in glycolytic capacity. High-uptake T cells exhibit an increase in both glycolytic and overall energetic capacities. Similarly, the mixed, unsorted splenocyte population demonstrates a more energetic phenotype, while maintaining a balance between glycolytic and oxidative pathways. These metabolic characteristics of naïve and activated T cells are in line with what is known from previous literature.[26–29]

For naïve cells (Figure 4B), low-uptake T cells show a minimal reliance on glycolysis, with approximately 3.3% of their energy resulting from glycolytic pathways. In contrast, high-uptake cells present with a significantly greater glycolytic reliance at around 66%. This increased glycolytic reliance of high-uptake T cells corresponds with the previous observations that these cells exist in an inherently more effector-like state than the low-uptake T cells.

In the activated cells (Figure 4C), the low-uptake T cells display a significant increase in glycolytic capacity compared to their naïve counterparts, rising to approximately 46.3%. High-uptake T cells maintain a similar reliance on glycolysis as in their naïve state, at around 47.8%, reflecting a metabolic phenotype characterised by an almost equal reliance on glycolysis and OXPHOS. Interestingly, no change in the glycolytic reliance for the high-uptake cells was observed here, indicating that the *in vitro* activation of these cells somehow overrides the metabolic differences observed in the naïve state.

While naïve cells show a more pronounced shift between OXPHOS and glycolysis, it’s important to note that their energy maps display smaller differences between low and high uptake conditions. This apparent contradiction is due to the overall low metabolic output (both mitochondrial and glycolytic ATP) in naïve cells. Although the shift seems minor in absolute terms, it represents a significant percentage of the total ATP output. In contrast, activated cells present a different scenario. The apparent difference in energy maps between low and high uptake conditions primarily reflects the lower overall ATP production in low uptake cells, rather than fundamentally different metabolic patterns. Both high and low uptake activated cells maintain similar levels of OXPHOS and glycolysis. However, high uptake cells generate substantially more ATP, indicating higher metabolic activity.

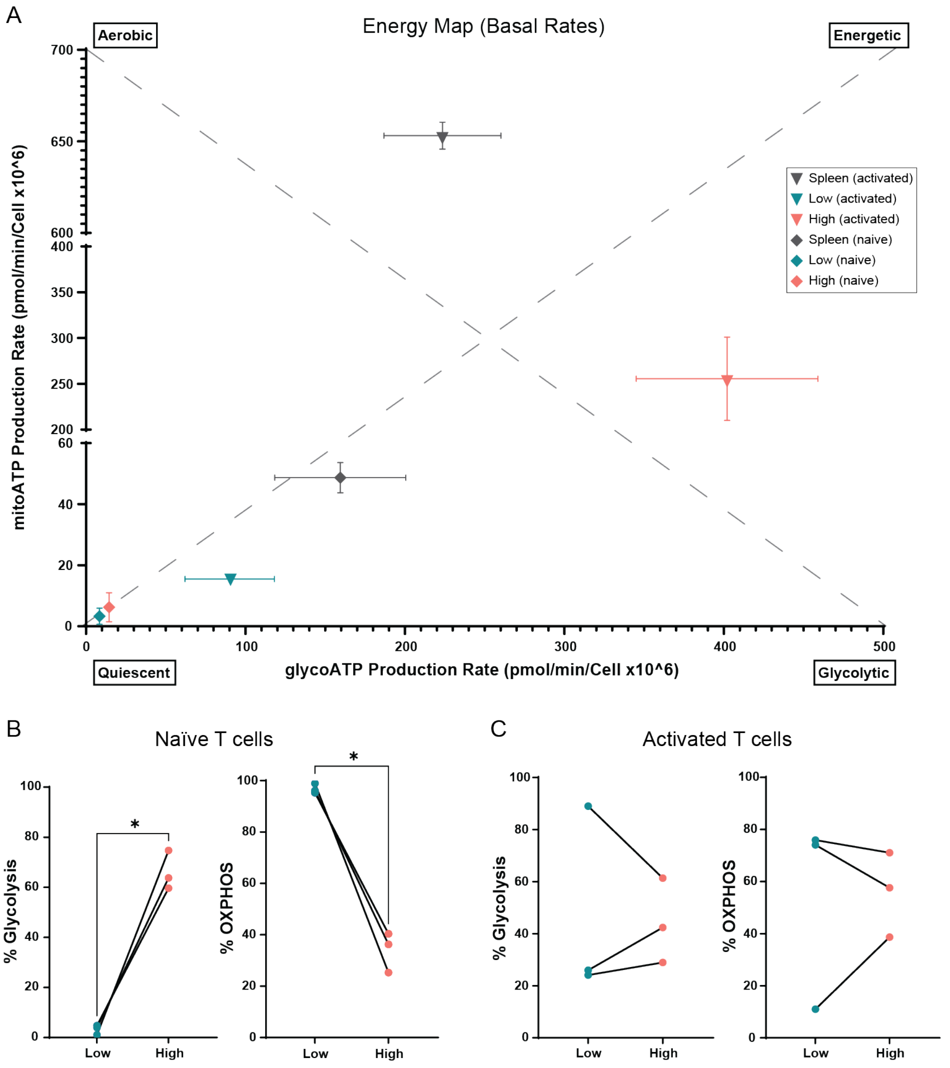

***Figure 4:** Metabolic bioenergetics of CD3+/CD4+ T cells following StA uptake and cell sorting to high (pink) and low (blue) uptake. **A)** Energy map, MitoATP versus GlycoATP of the naïve and activated cells. **B)** Naïve T-cell high and low uptake of StA showing % glycolysis reliance, and % OXPHOS (Wilcoxons). **C)** Activated T-cell high and low uptake of StA showing % glycolysis reliance, and % OXPHOS (Wilcoxons).*

Proteomic differences between T cells with differential StA-uptake

It has already been suggested that CD4+ T cells with a high StA uptake have a more effector-like phenotype compared to low-uptake cells. This is exemplified by increased cell size (Figure 2), increased CD44 expression (Figure 3), decreased CD62L expression (Figure 3), as well as increased metabolic activity (Figure 4). To investigate if these phenotypic differences were rooted in differences at the proteomic level, a chemical proteomics approach was applied to study the T cells with a differential StA uptake. Similarly to the metabolic energetics, CD4+ T cells with differential StA uptake were sorted by FACS (Figure S1). The sorted cells were then lysed to isolate the cellular proteins, followed by tryptic digestion of the proteins into shorter peptide chains, and LC-MS/MS analysis.[30] The processed proteomics data were analysed using R Statistical Software.[31] Proteins were identified as significantly up- or downregulated in the high-uptake population if they had a log2 fold change >1 or <-1, respectively, as well as a p-value <0.05. To further investigate the metabolic bioenergetic shifts that were observed, proteins linked to metabolic alterations were focused upon.

At a first glance, the principal component analysis (PCA) based on the results from the naïve CD4+ T cells shows that the four replicates were quite different from each other (Figure 5A). Instead of the high- and low-uptake samples clustering together, there is a stronger tendency of the replicates clustering together. This indicates that most of the variance in the data is between replicates, and not between the experimental conditions (low- or high-uptake). Keeping this limitation in mind, the samples were assessed further, and a total of 4141 unique proteins were detected in the naïve samples. However, only 23 proteins were differentially expressed (22 upregulated and 1 downregulated in the high-uptake population, Table S1). The heatmap (Figure 5B) and volcano plot (Figure 5C) show the expression levels of the differentially expressed proteins (DEPs). The low number of DEPs could be explained by the discrepancies observed in the PCA.

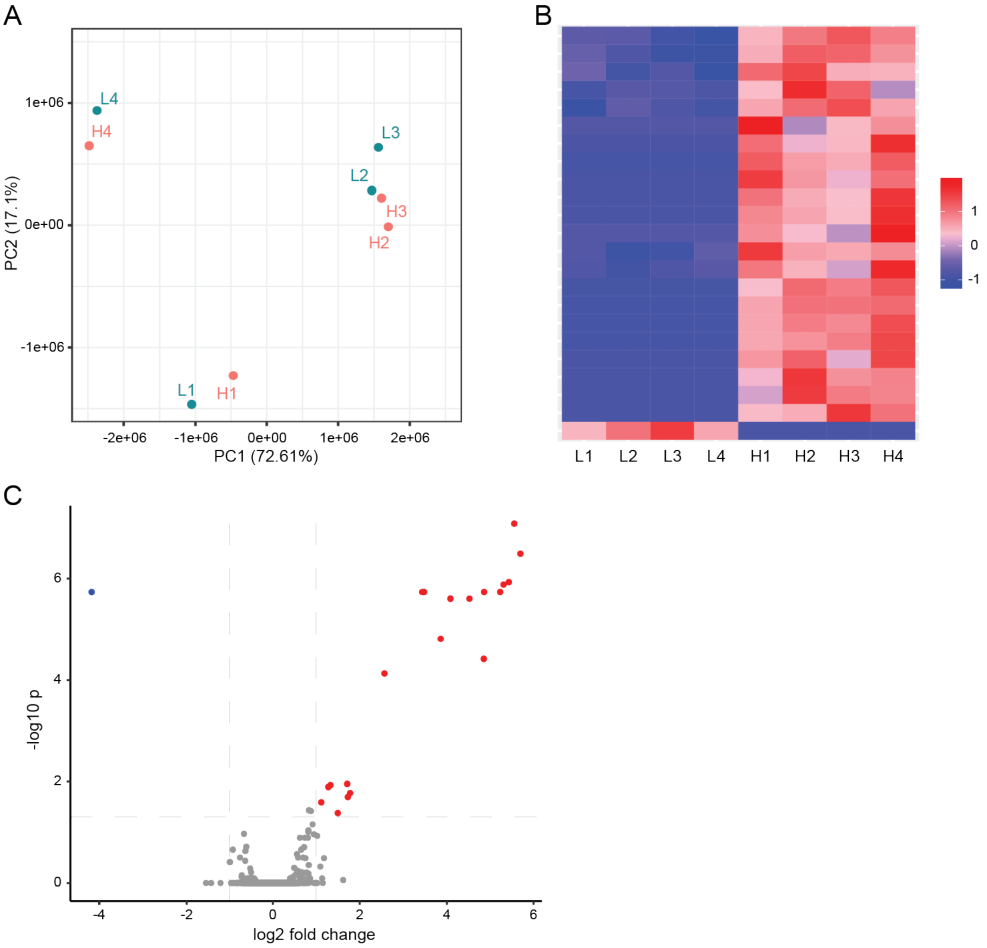

Figure 5: *Proteomics results from naïve CD3+/CD4+ T-cells,* ***A)*** *principal component analysis (PCA),* ***B)*** *heatmap,* ***C)*** *volcano plot. Red = upregulated, blue = downregulated. Based on 4 biological replicates.*

Among the DEPs, a few of the proteins were known to be involved in the proliferation and differentiation of CD4+ T cells. CDK1 and CD74 were upregulated in the high-uptake population (Figure 6A), where cyclin-dependent kinase 1 (CDK1) is a known regulator of the cell cycle, which drives cells through the G2 phase and mitosis.[32] In T cells, the CDK cascade has been proposed as a potential link between cell division and T cell differentiation via the phosphorylation of immunologically relevant transcription factors.[33] The upregulation of this protein in high StA-uptake T cells could indicate that the cells were in a more proliferative state than the low-uptake cells. While CD74 is mainly known as the invariant chain[34], which plays an important role in antigen presentation, recent research has also highlighted its role in T cell biology.[35–37] It has been shown to act as a receptor for the pleiotropic cytokine macrophage migration inhibitory factor (MIF), and is upregulated on the surface of activated CD4+ T cells supporting their migration.[38] CD74 has also been shown to be upregulated on tumour-infiltrating Tregs, where it facilitates accumulation and function of these cells via stabilising FOXP3 expression.[39] The upregulation of CD74 in high-uptake CD4+ T cells could thereby indicate an increased proportion of activated cells, and potentially also Tregs, in this population. This is in line with previously observations from this Chapter.

Additionally, F-box only protein 7 (FBXO7), a known cell cycle regulatory protein[40], is downregulated in the high StA-uptake CD4+ T cells. The downregulation of FBXO7 has previously been shown to increase glycolysis in CD4+ T cells[41], which could help explain the observed increase in glycolysis in the high-uptake population (Figure 4B).

Looking at the other DEPs, no metabolic proteins related to glycolysis, the tricarboxylic acid (TCA) cycle, or lipid metabolism, as annotated by UniProt[42] keywords KW-0324, KW-0816, and KW-0443, respectively, were detected in the naïve samples. The UniProt protein database categorises protein entries into specific subsets based on for example biological function or cellular localisation.[42] From the pathway analysis (Figure 6B), using the clusterProfiler package[43] in R, it is clear that the proteins that were upregulated in the high-uptake T cells are mainly involved in chromosome condensation and segregation. This indicates that the high-uptake cells were in a more proliferative state where the chromosomes are duplicated and separated during mitosis, compared to the low-uptake cells.

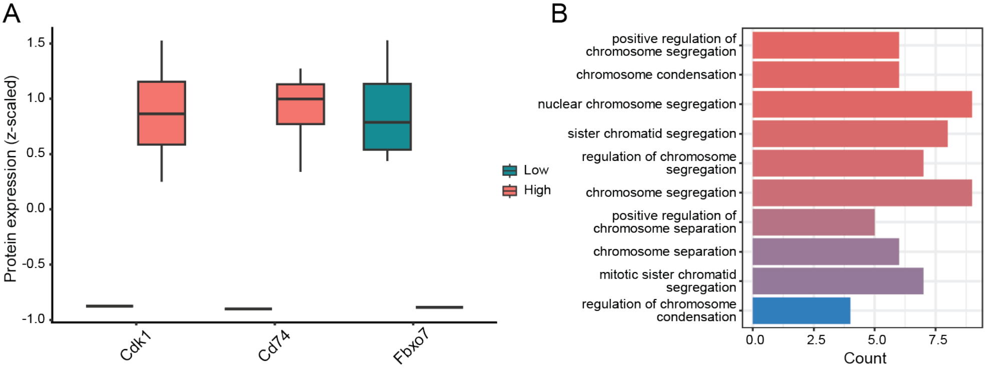

Figure 6: *Proteomics results from naïve CD3+/CD4+ T-cells,* ***A)*** *box plots of differentially expressed proteins that are involved in T cell biology,* ***B)*** *pathway analysis of all upregulated proteins (using the clusterProfiler package[43] in R). Based on 4 biological replicates.*

This data suggests two things. Firstly, the biology that underpins the changes in FA uptake in the naïve population may be stochastic in nature, rather than being fully reliant on pre-existing phenotypic differences between the cells. The second observation is that the naïve cells that take up more FA are in higher state of cell division, suggesting the presence of background T cell replication even in naïve unstimulated populations.

The same cell sorting and proteomic approach was applied to CD4+ T cells that had been activated in vitro using αCD3/αCD28 antibodies prior to StA uptake. The PCA following subsequent examination of the activated CD4+ T cells, shows a better separation between the low- and high-uptake conditions, and a better clustering of the respective replicates (Figure 7A). This is also reflected in the heatmap

(Figure 7B) and volcano plot (Figure 7C) where it is apparent that more proteins were differentially expressed than for the naïve samples. Of in total 4956 unique proteins that were detected, 358 were differentially expressed for the activated cells. Of the DEPs 204 were downregulated and 154 were upregulated in the high-uptake samples (Table S2).

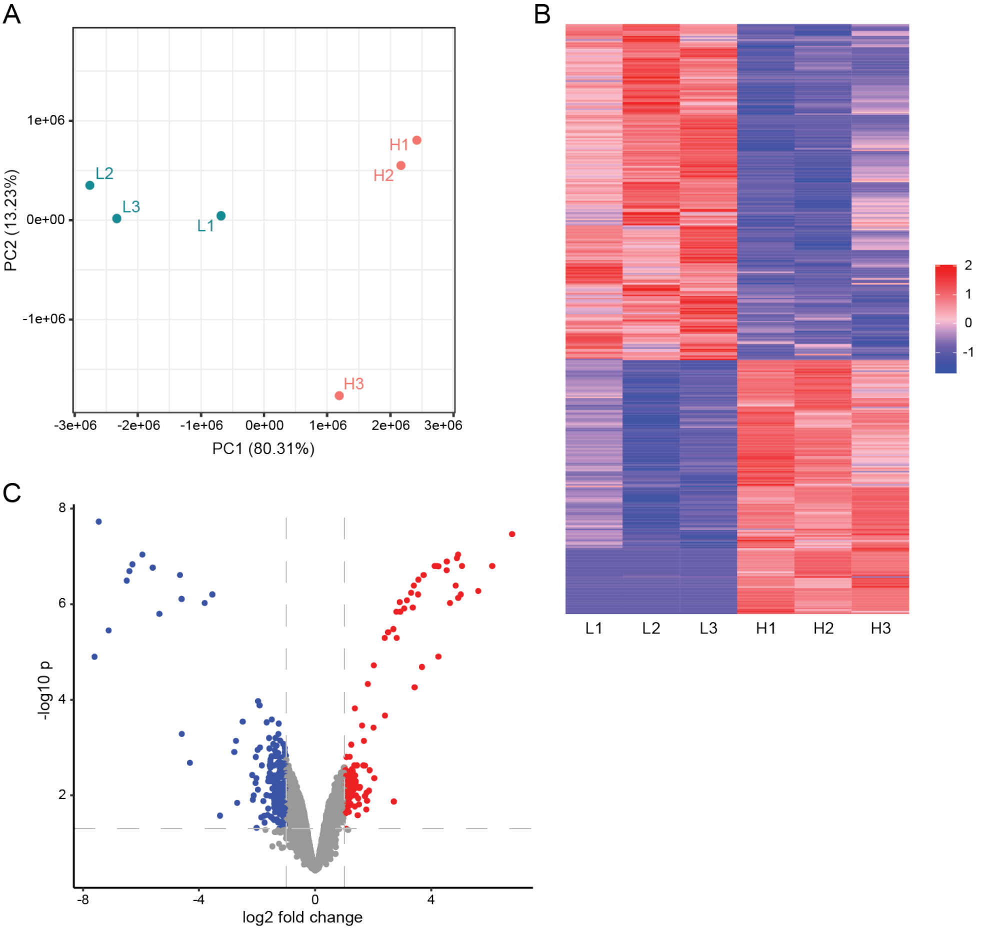

Figure 7: *Proteomics results from αCD3/αCD28-activated CD3+/CD4+ T-cells,* ***A)*** *principal component analysis (PCA),* ***B)*** *heatmap,* ***C)*** *volcano plot. Red = upregulated, blue = downregulated. Based on 3 biological replicates.*

Several proteins involved in cellular metabolism were identified as differentially expressed in the activated CD4+ T cells (Figure 8A). This includes HK2 and IRF4 which are involved in glucose metabolism. Hexokinase 2 (HK2) is the first rate-limiting step of glucose metabolism, phosphorylating glucose to glucose-6-phosphate.[44] Upon T cell activation, HK2 is known to be upregulated to support the increased metabolic requirements of these cells.[45–47] Interferon regulatory factor 4 (IRF4) has been implicated as an important transcription factor involved in the differentiation of T cell subsets upon activation, as well as controlling the metabolic shift of activated T cells.[48–51] It has even been proposed that IRF4 controls the expression of glycolytic enzymes, there among HK2.[48]

Several proteins involved in fatty acid synthesis were also upregulated in the high StA-uptake, activated T cells (Figure 8A). The three proteins ATP citrate lyase (ACL, encoded by the gene *ACLY*), acetyl-CoA carboxylase (ACC1, encoded by the gene *ACACA*), and fatty acid synthase (FAS, encoded by the gene *FASN*) catalyse the *de novo* biosynthesis of palmitic acid from citrate, a product of the TCA cycle.[52,53] All three proteins were upregulated in the high StA-uptake T cells. The genes encoding these proteins have previously been reported to be upregulated in activated T cells[6,8,54], thereby supporting the current observations that the high-uptake CD4+ T cells take on a more activated phenotype.

The high StA-uptake T cells thereby appear to have an increased flux through glucose metabolism (as indicated by the upregulation of IRF4 and HK2), potentially to fuel the production of citrate and subsequent *de novo* fatty acid synthesis (via ACL, ACC1 and FAS), which fits the observations of the metabolic extracellular flux experiments (Figure 4).

Additionally, a number of proteins of the mevalonate pathway, where mevalonate is formed from HMG[55], were found to be upregulated in the high-uptake CD4+ T cells (Figure 8A). In the mevalonate pathway acetyl-CoA is turned into dimethylallyl pyrophosphate (DMAPP), which is further metabolised into geranyl pyrophosphate (GPP) and farnesyl pyrophosphate (FPP) via the enzyme farnesyl pyrophosphate synthase (FDPS).[56,57] FPP is a precursor for multiple other biosynthetic pathways such as cholesterol[58], ubiquinone[59], and dolichol[60] biosynthesis, as well as protein prenylation.[61] The proteins hydroxymethylglutaryl (HMG)-CoA synthase 1 (HMGCS1), phosphomevalonate kinase (PMVK), and isopentenyl-diphosphate delta isomerase 1 (IDI1) are all involved in different parts of this pathway. The mevalonate pathway is important for T cell activation and differentiation because it leads to increased cholesterol biosynthesis[62,63], ensuring sufficient production of an indispensable membrane component, especially during proliferation. Additionally, cholesterol is enriched in the immunological synapse and is essential for its proper function.[64–66] The upregulation of key enzymes in this pathway therefore further supports that high-uptake CD4+ T cells are more effector-like cells than the low-uptake cells.

The pathway analysis of DEPs in activated CD4+ T cells (Figure 8B), using the clusterProfiler package[43] in R, showed an upregulation of pathways involved in ribosomal biogenesis and protein translation in the high-uptake cells. This indicates a large general biosynthetic focus of these cells, which also fits with the previously described observations that the high-uptake cells were in a more effector-like or activated state.

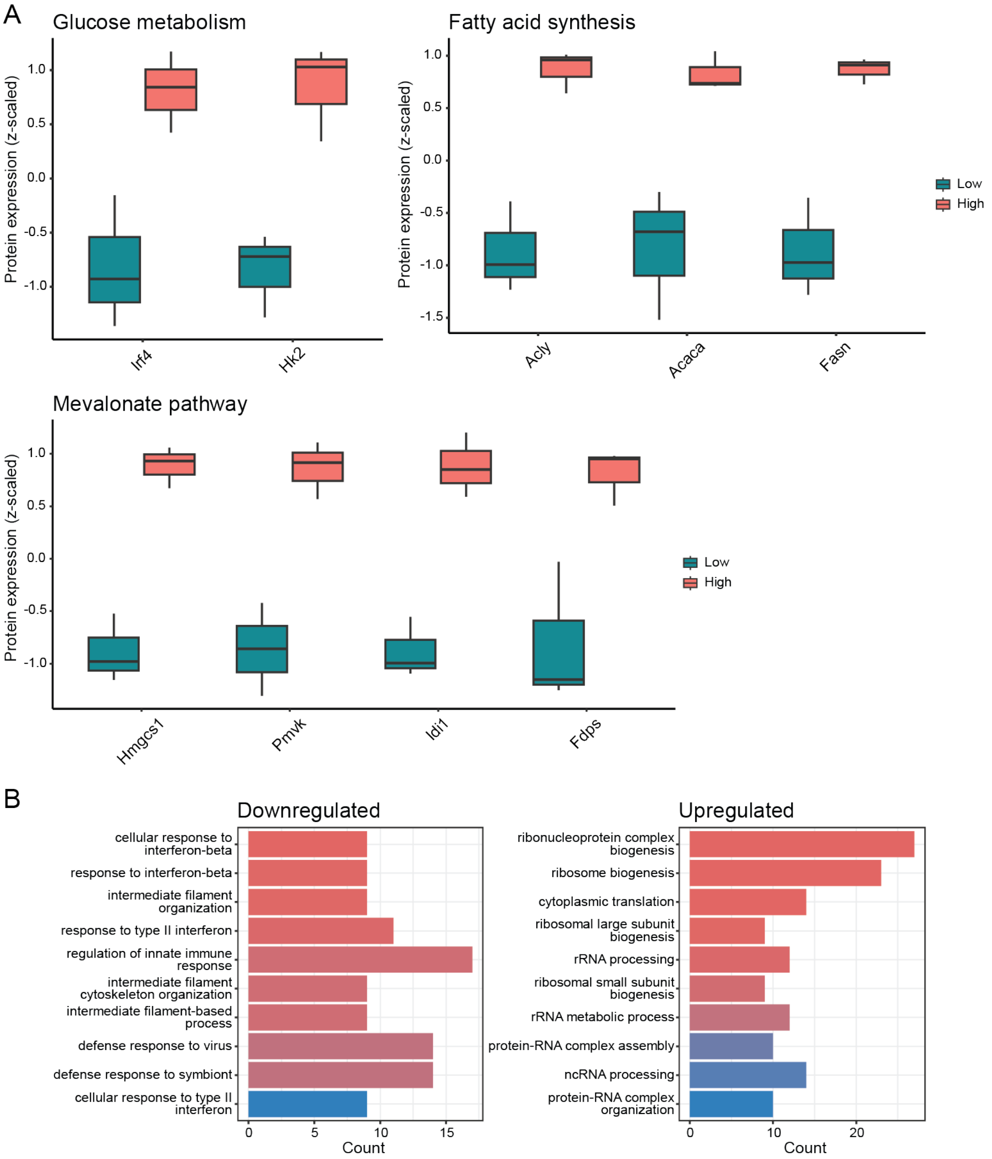

***Figure 8:** Proteomics results from αCD3/αCD28-activated CD3+/CD4+ T-cells, **A)** box plots of significantly upregulated proteins that are involved in glucose metabolism, fatty acid synthesis, and the mevalonate pathway, **B)** pathway analysis of the downregulated and upregulated proteins separately (using the clusterProfiler package[43] in R). Based on 3 biological replicates.*

Single-cell RNA sequencing of splenocytes with differential StA-uptake

To complement the chemical proteomics data, and to gain further insight into how different immune cell subsets react to differential StA uptake, a single-cell RNA sequencing (scRNAseq) approach was also developed, using the 10x Genomics platform.[67] scRNAseq was chosen over bulk RNAseq due to the heterogeneity of the splenocyte population. However, since the splenocytes had to undergo an IEDDA click reaction prior to FACS, it was essential to ensure that the click reaction did not impact the integrity of the unstable RNA molecules.

Therefore, cells were treated with StA (or DMSO vehicle), before IEDDA reaction with fluorophore **7** was performed on either live, or fixed and permeabilised cells. The total cellular RNA was isolated from these samples and separated on agarose gel to visualise RNA integrity. Since cellular RNA consists mainly of ribosomal RNA (rRNA, 80-90%), the 28S and 18S rRNA subunits are the two bands that will be visible on the agarose gel, in a 2:1 ratio. When isolating RNA from fixed cells, a slight shift in the bands were visible compared to live cells, but there was no visible change in RNA integrity upon addition of StA, or after the IEDDA click reaction (Figure S2A). In contrast, the addition of oleic acid analogues containing alkyne or azide modifications (Figure S2D), and subsequent copper-catalysed azide-alkyne cycloaddition (CuAAC), showed visible RNA degradation (Figure S2B). To determine which component of the CuAAC mixture caused this degradation, each component was tested individually (Figure S2C). Only upon addition of the complete CuAAC mixture to the cells, RNA degradation occurred, implying that the active copper(I) species in the mixture, which is only present after reduction with sodium ascorbate, is responsible for the degradation. These results further demonstrate the benefits of using the IEDDA click reaction when studying unstable biomolecules such as RNA.

Taking advantage of the demonstrated RNA integrity after IEDDA click reaction, the scRNAseq approach was applied to study the transcriptomic differences on a complete splenocyte level, between the sorted high and low StA-uptake cells. The gating strategies for sorting naïve and αCD3/αCD28 activated splenocytes are shown in Figure S3.

The populations with the lowest and highest quartile of StA uptake, which were collected by FACS, were analysed using a 10x Genomics scRNAseq workflow in collaboration with the Leiden Genome Technology Center (LGTC). Upon quality control of the sequencing data, it was discovered that one sample, the high-uptake sample from naïve splenocytes, had significantly higher RNA counts per cell than the other samples (Figure S4). In fear of the high RNA counts from this sample skewing the data, the high- and low-uptake samples from naïve splenocytes were omitted from the remaining analysis. Further analysis was only performed on the high- and low-uptake samples from activated splenocytes.

The cells from the samples with activated splenocytes were clustered based on their gene expression. The resulting UMAP highlights substantial differences between the low- and high-uptake samples (Figure 9), where certain cell clusters are differentially present in the different uptake conditions.

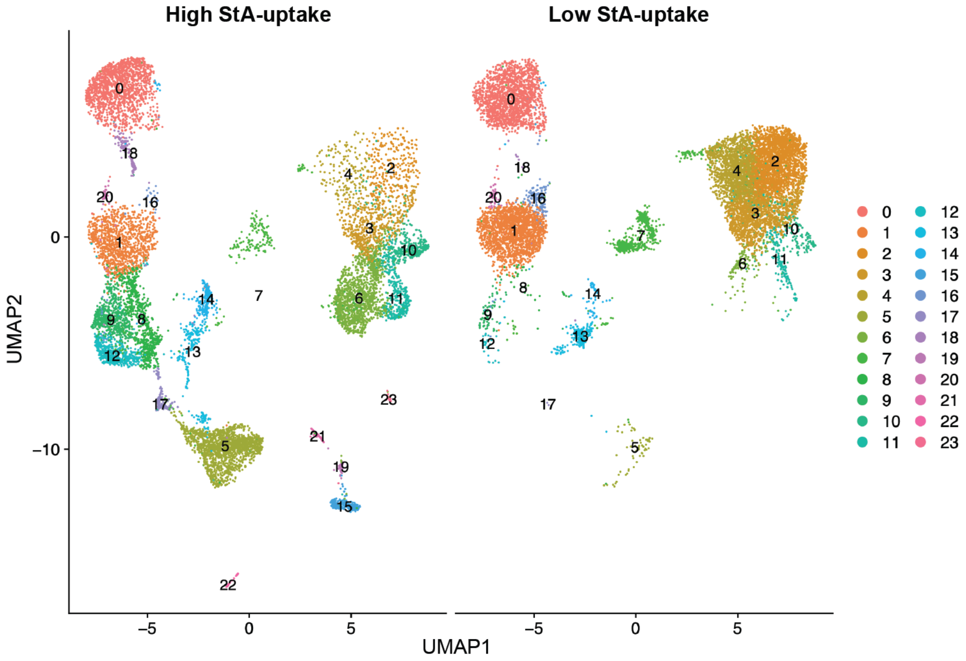

Figure 9: *UMAP showing cell clustering based on gene expression from high- and low-StA uptake samples of activated splenocytes. The data is based on scRNAseq results.*

Identification of the immune cell subsets corresponding to each cluster was done according to expression of relevant marker genes (Tables 1 & S3). This highlights that B cells (clusters 2-4, 6, 10-11) were mainly present in the low-uptake sample, whereas certain T, NKT, or NK cell clusters were mostly present in the high-uptake samples (clusters 5, 8-9, 12, 14, 18) or equally present in both low- and high-uptake samples (clusters 0-1, 13).

Table 1: *Immune cell subsets corresponding to clusters identified from the scRNAseq analysis (from Figure 2). Relevant marker genes for the identification can be found in Table S3.*

Cluster	Subset	Cluster	Subset	Cluster	Subset
0	CD4+ T cells	**8**	CD8+ T cells	**16**	CD8+ T cells
1	CD8+ T cells	**9**	CD8+ T cells	**17**	Mixed
2	B cells	**10**	B cells	**18**	CD4+ T cells
3	B cells	**11**	B cells	**19**	Monocytes
4	B cells	**12**	CD8+ NKT cells	**20**	Mixed
5	NK cells	**13**	CD4+ NKT cells	**21**	Monocytes
6	B cells	**14**	CD4+ Treg	**22**	NK cells
7	Mixed	**15**	Monocytes	**23**	Monocytes

From the FACS data, it was clear that the activated cells, and especially those taking up large amounts of StA, were larger (as seen by FSC) and more granulated (as seen by SSC), than the naïve and low-uptake cells (Figures 10A & 10B). Since the activated high-uptake population consists of a larger portion of NK cells and CD8+ T cells, and these cell types are known to match this morphology[22,23], this could help explain these differences. The low-uptake population consists of more B cells, which were not targeted by the αCD3/αCD28 activation, and could therefore explain why these cells appear smaller and less granulated. When the splenocytes were activated, the BODIPY signal is more widely distributed (Figure 10C), implying that there is more spread in the StA-uptake in these cells than for the naïve splenocytes.

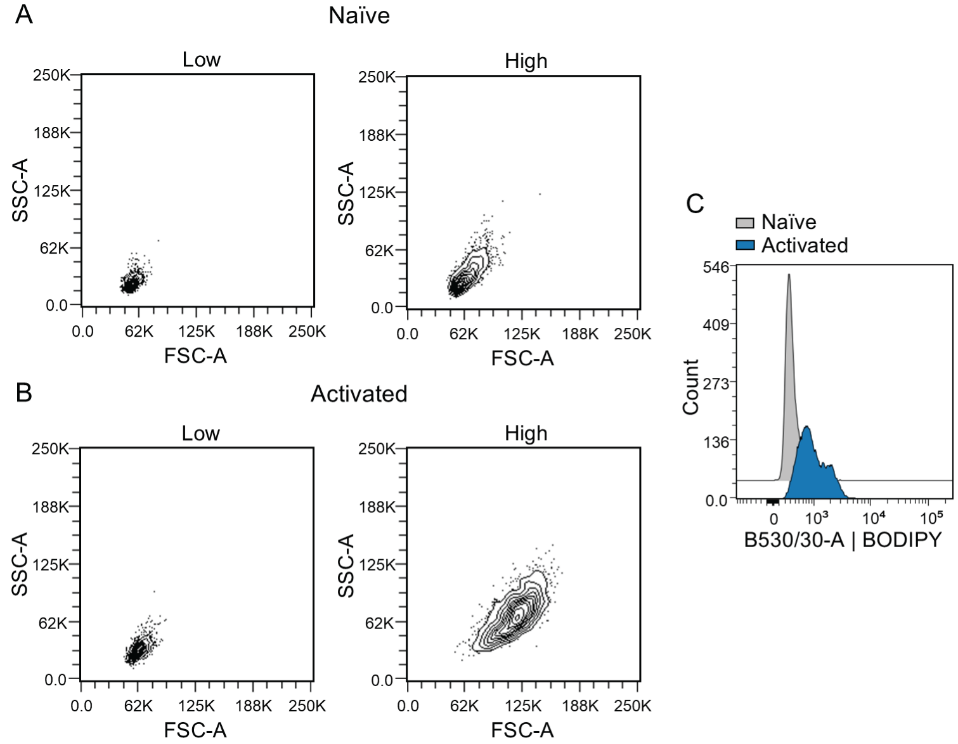

Figure 10: *High-uptake cells are bigger and more granulated, especially in activated splenocytes. Based on forward scatter (FSC) and side scatter (SSC) of cells after sorting them into high- and low-StA uptake populations for scRNAseq of* ***A)*** *naïve splenocytes,* ***B)*** *αCD3/αCD28-activated splenocytes,* ***C)*** *Histogram showing the BODIPY signal (indicating StA uptake) of naïve or activated splenocytes (according to the gating strategies shown in Figure S2).*

The focus of this section is on lymphocytes, and more specifically T cells, NKT cells, and NK cells. Superimposing the expression of the genes encoding the subunits of T cell co-receptor CD3 (*CD3E*, *CD3D*, and *CD3G*) onto the scRNAseq UMAP (Figure 11A), shows that different T cell subsets (CD4+, CD8+, Treg), as well as NKT cell subsets (CD4+, CD8+) express this pan T cell marker. Performing the same overlay with the T helper cell marker CD4 (*CD4*, Figure 11A), highlights the same clusters that were identified as CD4+ in Table 1, validating that approach. Focusing on the clusters containing T, NKT, and NK cells (Figure 11B), again emphasises that NK cells, regulatory T cells (Tregs), and certain CD8+ T and NKT cell subsets were mainly present in the high-uptake population, CD4+ T cells and certain subsets of CD8+ T cells were similarly present in both, whereas CD4+ NKT cells were mainly present in the low-uptake population.

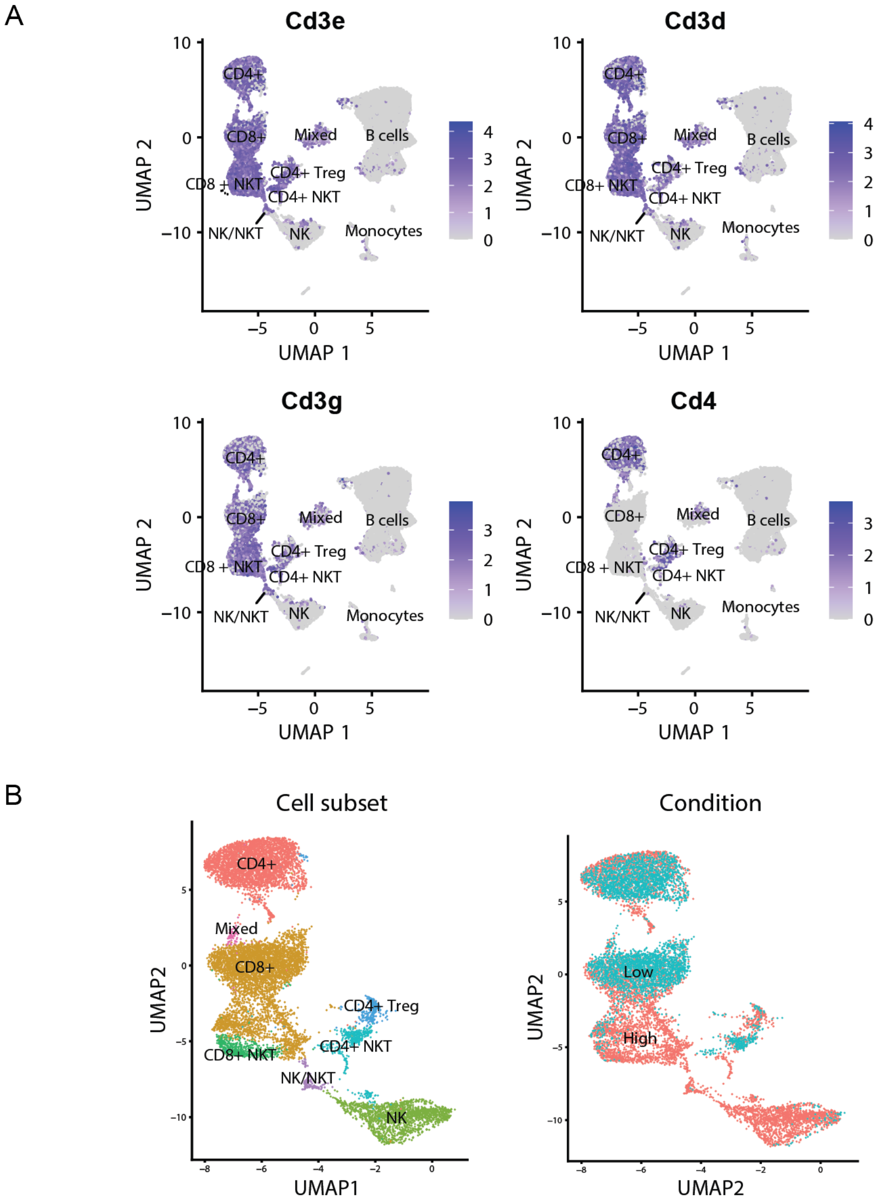

Figure 11: *Subsections of the scRNAseq UMAP showing* ***A)*** *clusters expressing the genes encoding CD3 subunits (CD3E, CD3D, CD3G) and CD4,* ***B)*** *zoom-in on clusters of interest containing T, NKT, and NK cell (lymphocyte) subsets.*

All the highlighted lymphocyte subsets can be categorized by their own distinct metabolic features to support their immunological functions. Conventional CD4+ or CD8+ T cells change their metabolic requirements upon activation.[3,68–71] While naïve or memory T cells rely heavily on FAO and OXPHOS to support their energetic needs, they undergo a switch to a highly glycolytic state, with increased *de novo* fatty acid synthesis, upon activation and differentiation into effector T cells. All these T cell subsets were included in the CD4+ and CD8+ clusters in Figures 9 & 11, and the wide metabolic range of these T cell subsets can explain the spread in observed StA-uptake by these cells.

NK cells are known to rely heavily on fatty acid uptake and FAO to fuel their effector functions[72,73], which could explain why they were mainly detected in the high StA-uptake population. Previous research has also put fatty acid uptake and FAO at the centre of Treg differentiation and function.[74–76] This is further supported by the localisation of Tregs mainly in the high StA-uptake population (Figures 9 & 11). While NKT cell development has been reported to require lipids[77], and *de novo* fatty acid synthesis is implicated in maintaining NKT cell homeostasis[78], not much is known about the uptake and metabolism of exogenous fatty acids in this cell type. No logical explanation can therefore be given to the observed discrepancy in StA-uptake between CD4+ (low uptake) and CD8+ (high uptake) NKT cells (Figures 9 & 11).

After selecting the clusters containing the lymphocyte subsets of interest, the focus was shifted to the expression of key metabolic genes involved in lipid metabolism and glycolysis in these clusters. These metabolic pathways were chosen because they are known to be differentially expressed, and utilised, by different lymphocyte subsets.[26–29] The expression of the relevant genes can be seen in Figures S5 & S6 and Figures S7 & S8, for lipid metabolism and glycolysis, respectively. It became clear that the expression of most of the genes were equally distributed across clusters, and show little differential expression based on differential StA uptake. However, some differentially expressed genes could be detected. For genes involved in fatty acid metabolism, *FASN*, *HMGCR*, and *CCR5* appear to be upregulated in the high-uptake cells (Figure 12A). This upregulation occurred across almost all the lymphocyte subsets (Figure 12B).

As previously explained, *FASN* encodes the enzyme fatty acid synthase (FAS) which catalyses the *de novo* synthesis of palmitic acid (C16:0) from acetyl-CoA and malonyl-CoA.[79] *De novo* fatty acid synthesis, and *FASN* specifically, has been shown to be necessary for the metabolic reprogramming of activated T cells.[6,8] *HMGCR* encodes HMG-CoA reductase, the enzyme catalysing the rate-limiting step of the mevalonate pathway, where mevalonate is formed from HMG.[55] *HMGCR* has been shown to be indispensable for T cell survival[80] and activation[81], and has also been shown to play a significant role in the cytotoxic activity of NK cells.[82] The upregulation of *FASN* and *HMGCR* could therefore indicate that the high StA-uptake cells were in a more activated state than the low-uptake cells. These results are in line with the observations that were made when looking at the proteomic differences between high and low StA-uptake populations (Figure 8A).

CCR5 encodes CC chemokine receptor 5, a receptor that can bind a number of chemokines such as CCL3, CCL4, and CCL5.[83] In NK and NKT cells, where this gene is mainly expressed (Figure 12B), *CCR5* has been shown to be important for proper trafficking and function of these cells.[84,85]

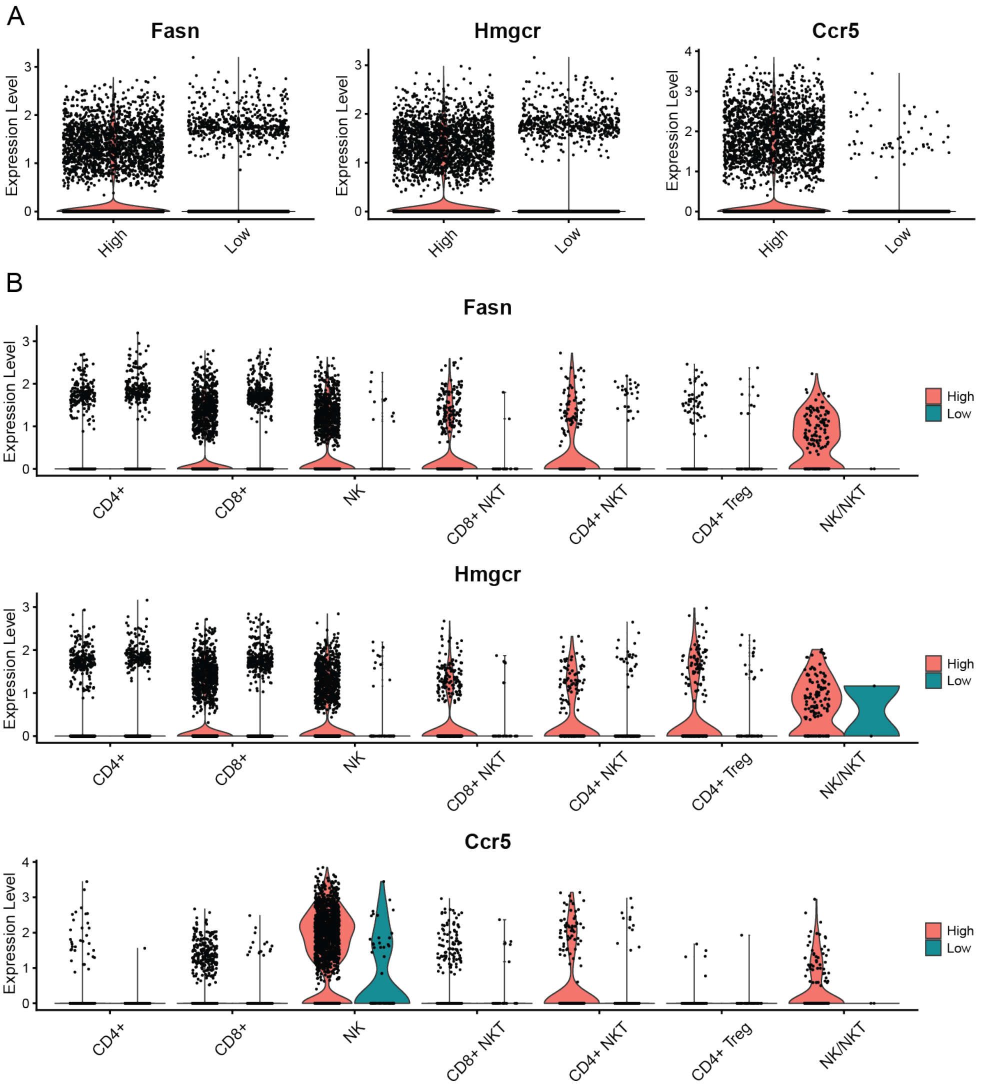

Figure 12: *Differentially expressed genes related to lipid metabolism from scRNAseq in the high- and low-uptake populations of T, NKT, and NK cells (lymphocytes), represented as violin plots.* ***A)*** *pooled data from all the relevant lymphocyte clusters,* ***B)*** *showing the data for the lymphocyte clusters separately.*

For the scRNAseq data presented here, it is important to note that the high-uptake cells were overrepresented in some clusters (e.g. CD8+ T cells, CD8+ NKT cells, and NK cells). This results in fewer data points for the low-uptake cells and could skew the data in the direction of genes appearing upregulated in the high-uptake cells. It can therefore not be said with certainty that the mentioned proteins were upregulated.

When focusing on genes involved in glycolysis, *LDHA*, *SREBF1*, *PIK3CA*, and *AKT2* appear to be upregulated in the high StA-uptake cells (Figure 13A). The upregulated genes were observed in almost all the lymphocyte subsets (Figure 13B).

LDHA encodes the enzyme lactate dehydrogenase A (LDHA) which is responsible for the last step of glycolysis where pyruvate is converted to lactate.[86] The deletion of *LDHA* has previously been shown to suppress glycolysis rates, as well as T cell proliferation and differentiation.[87] Similarly, effector T cells showed increased expression of *LDHA*, as a result of phosphoinositide-3-kinase (PI3K) signalling.[86] Here, the increased expression of *LDHA* could indicate an increased effector-like function of the high StA-uptake cells. This is further supported by the upregulation of *PIK3CA* and *AKT2*, genes encoding the catalytic PI3Kα subunit, and RAC-beta serine/threonine-protein kinase (AKT2), respectively. The PI3K-AKT axis has been implicated as an important signalling pathway for metabolic reprogramming in activating and differentiating T cells[88–90], and could explain the upregulation of *LDHA*, as well as indicating that the high-uptake cells have undergone this metabolic reprogramming into proliferating, highly glycolytically active cells. Interestingly, it appears that *PIK3CA* is downregulated in high StA-uptake Tregs, in contrast to all the other lymphocyte clusters where it is upregulated (Figure 13B). The reliance of Treg function and differentiation on PI3K is debated, and PI3K has been shown to both inhibit and support the development of this T cell subset.[91–94] Therefore, it is not clear what the downregulation of *PIK3CA* in Tregs mean for their function in this case. In addition, it is not clear why only *PIK3CA*, and not *PIK3CB* and *PIK3CD* encoding the PI3K β and δ subunits, respectively, is differentially expressed in this data (Figure S8), especially since *PIK3CD* is known to be the most prevalent subunit class in T cells.[95] It is also not clear why *AKT2* is differentially expressed, but not its isoforms *AKT1* and *AKT3* (Figure S8).[96] Downstream targets of the PI3K/AKT pathway, such as *MTOR*, *FOXO1*, and *MYC*[97], were also not differentially expressed upon StA uptake in this experiment.

SREBF1, a gene downstream of the PI3K/AKT signalling pathway[98,99], also plays an important role in the metabolic reprogramming in the activation phase of T cells.[8] The gene encodes the transcription factor sterol regulatory element-binding protein 1 (SREBP1), that induces the expression of all genes involved in *de novo* fatty acid and cholesterol synthesis.[8,100,101] The upregulation of this gene could help explain the observed increase in *FASN* and *HMGCR* (Figures 12A & 12B) that was described earlier. In addition, *SREBF1* has also been shown to influence the expression of glycolysis-related genes[102,103], and could together with the increase in *LDHA*, *PIK3CA*, and *AKT2* indicate that the high-uptake cells were more glycolytically active, and thereby more activated or effector-like, in line with the previous results discussed in this Chapter.

Thereby, the upregulation of the metabolic pathways appeared to be the result of increased expression of the PI3K-AKT signalling pathway, which in turn caused an upregulation of transcription factor SREBP1, known to modulate both glycolysis and lipid biosynthetic pathways.[8,104–107]

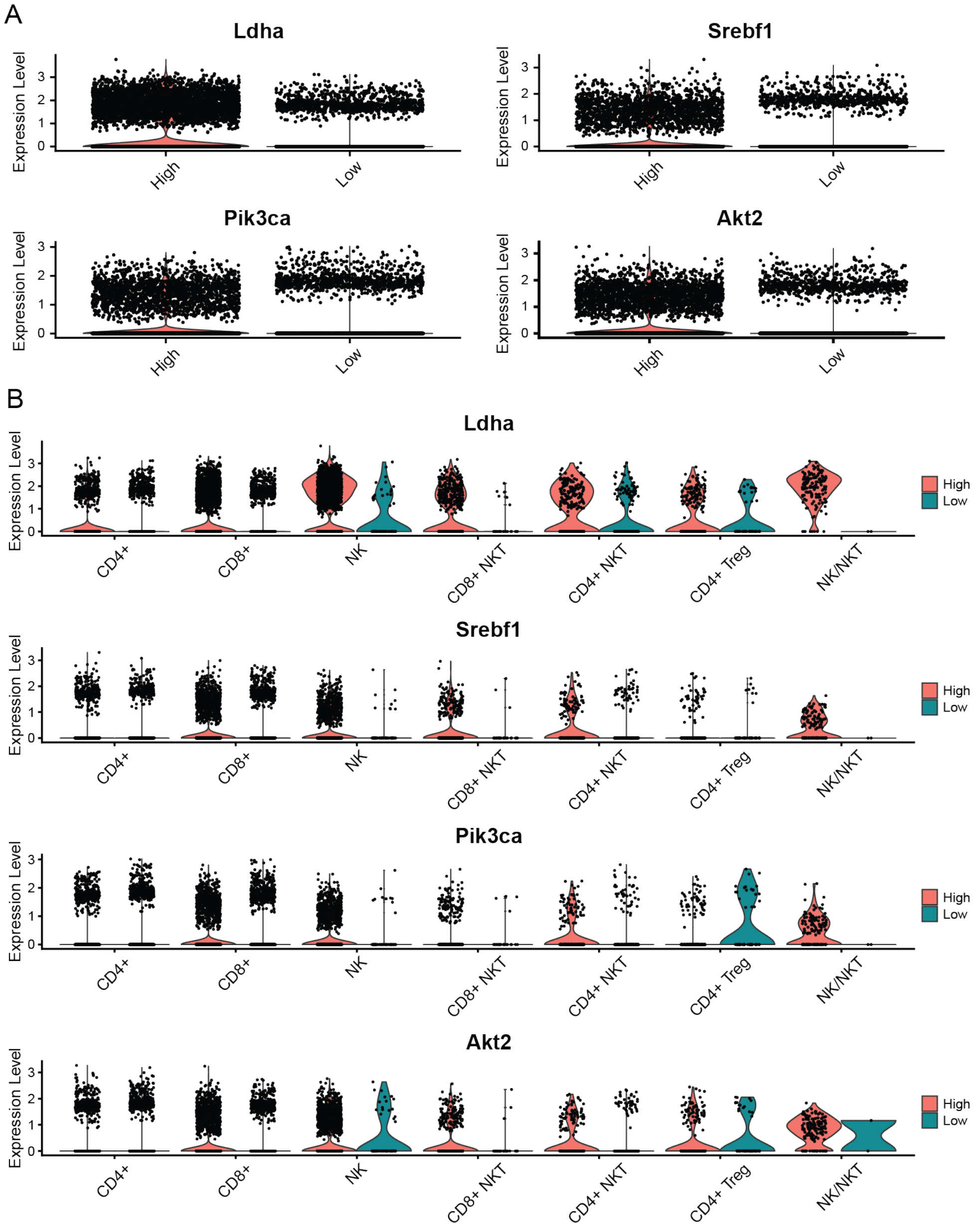

Figure 13: *Differentially expressed genes related to glycolysis from scRNAseq in the high- and low-uptake populations of T, NKT, and NK cells (lymphocytes), represented as violin plots.* ***A)*** *pooled data from all the relevant lymphocyte clusters,* ***B)*** *showing the data for the lymphocyte clusters separately.*

Since the scRNAseq data were based on only one biological replicate, it was not possible to do statistics on the expression levels of the relevant genes. To verify and strengthen the results, more replicates would be necessary. Due to cost- and time-restraints, this was not possible to accomplish within the scope of this project.

However, the results from the scRNAseq are in line with what was previously observed with proteomics, where glucose metabolism (via HK2), fatty acid synthesis (via ACL, ACC1, and FAS), and the mevalonate pathway (via FDPS, HMGCS1, PMVK, and IDI1) were also upregulated in the activated, high-uptake CD4+ T cells. This strengthens the observations made by the two different methods, increasing the reliability of the data.

While the metabolic energetics, as determined by Seahorse extracellular flux analysis, showed a significant increase in glycolytic reliance only in the naïve high StA-uptake cells (Figures 4B & 4C), proteomics (Figure 8A) and scRNAseq (Figures 12 & 13) also indicated an increased flux through glycolysis, as well as fatty acid synthesis and the mevalonate pathway, which are derived from side products from glucose metabolism. In combination, this could indicate that also the *in vitro* αCD3/αCD28 activated cells showed increased glycolytic activity upon high StA-uptake.

This proof-of-principle Chapter has highlighted a connection between increased exogenous FA uptake, and increased metabolic activity and an effector-like phenotype. Previously, genes involved in *de novo* FA synthesis (*ACACA*, *FASN*) and the mevalonate pathway (*HMGCR*, *HMGCS1*, *FDPS*), as well as their regulator *SREPF1*, have been reported to be upregulated in CD4+ T cells treated with OA.[15] However, a lot is still unclear as to the exact mechanism behind these observations. Firstly, no changes in known fatty acid transport proteins such as CD36[108] or fatty acid-binding protein 5 (FABP5)[109] were detected in neither the scRNAseq data (Figure S6), nor the proteomics data (Tables S1 & S2). It is therefore not clear how exogenous StA is taken up by the cells. Additionally, these experiments cannot determine if the increased effector-like phenotype of the high-uptake cells is an inherent property, or if it is a response to the increased FA availability in the culture medium of the cells. Since the cells in most cases are pulsed with StA for only 15 minutes, the former is deemed most probable. However, further research is necessary to support this hypothesis.

Conclusion

In this Chapter, a workflow for multiplexing the uptake of bioorthogonal OA analogue, StA, with single-cell analytical methods like flow cytometry, and a multiomics approach, was developed. Populations of naïve T cells and T cells activated *in vitro* with αCD3/αCD28, with a high uptake of StA, were shown to take on a more effector-like phenotype compared to low StA-uptake cells. This was demonstrated by increased cell size, increased CD44 expression, decreased CD62L expression, increased glycolytic activity, as well as the upregulation of key metabolic pathways of effector T cells. Key genes involved in glycolysis, fatty acid synthesis, and the mevalonate pathway were upregulated in high StA-uptake splenocytes, as detected by scRNAseq. This analysis was focused on T, NKT, and NK cells. In addition, proteins in the same pathways were upregulated in CD4+ T cells as determined by proteomics, indicating robust results. It is not clear whether certain cells take up more exogenous StA because of an inherently more effector-like state, or if the high StA-uptake is induced by the increased availability of FAs in the culture medium. Further research is necessary to answer these questions.

Acknowledgements

The Leiden Genome Technology Centre (LGTC) at Leiden University Medical Centre (LUMC) are acknowledged for their help with scRNAseq sample preparation, sequencing, and data analysis. The Flow Cytometry Core Facility (FCF) at LUMC are acknowledged for their help with operating the FACS. Dr. Bogdan I. Florea, Dr. Berend Gagestein, and Dr. Joel Rüegger are acknowledged for their contribution with setting up a protocol for proteomics, as well as sample measurement and data processing. Dr. Graham Heieis and Dr. Bart Everts are acknowledged for their insightful input and ideas in the development of this project. Kas Steuten is acknowledged for providing murine spleens for the experiments. Dr. Laura Bogue Edgerton is acknowledged for assisting with FACS, Seahorse analysis, and preparation of proteomics samples. All the mice that were sacrificed for this research are acknowledged.

Materials & Methods

General. Sterculic acid was purchased from Cayman Chemical (#26735), and stored as 10 mM or 100 mM stock solutions in DMSO at -20°C. Oleic acid-alkyne (#900412E) and oleic acid-azide (#900415C) were purchased from Avanti, and stored as 10 mM stock solutions in DMSO at -80°C. Oleic acid was purchased from Sigma Aldrich (#O1383), and stored as 100 mM stock solution in DMSO at -80°C. AZDye 488 alkyne (#CCT-1277) and AZDye 488 azide (#CCT-1275) were purchased from Click Chemistry Tools (now VectorLabs), and stored as 2 mM stock solutions in DMSO at -20°C. Fluorophore **7** was synthesised in-house (see Chapter 2 of this thesis), and was stored as 2 mM stock solution in DMSO at -20°C. The murine RNase inhibitor was purchased from New England Biolabs (#M0314L), and stored as delivered at -20°C. Zombie NIR Fixable Viability kit was purchased from BioLegend (#423105), and stored as delivered at -20°C. DNase I was purchased from Thermo Fisher Scientific (#90083), and stored as delivered at -20°C. PE/Dazzle 594 anti-mouse CD3 antibody was purchased from BioLegend (#100246), and stored as delivered at 4°C. APC anti-mouse CD4 antibody was purchased from BioLegend (#100516), and stored as delivered at 4°C. eFluor450 anti-mouse CD44 antibody was purchased from Invitrogen (#48-0441-82), and stored as delivered at 4°C. PE-Cyanine7 anti-mouse CD62L antibody was purchased from Invitrogen (#25-0621-82), and stored as delivered at 4°C.

DC2.4 cell culturing. DC2.4 cells were cultured in RPMI 1640 culture medium (Gibco, #31870025) supplemented with 10% FCS, GlutaMAX (2 mM), sodium pyruvate (1 mM), 1x non-essential amino acids (NEAA, Thermo Fisher Scientific), penicillin (100 I.U./mL), streptomycin (50 μg/mL), and 2-mercaptoethanol (50 μM, Thermo Fisher Scientific), and incubated at 37°C, 5% CO_2. The cells were grown to 70-80% confluency and passaged every 2-3 days by trypsinisation.

Splenocyte isolation, stimulation and culturing. Spleens were harvested from naïve C57BL/6 mice. To obtain a single-cell suspension of splenocytes, the spleens were minced with the flat end of a syringe plunger over a 70 μm cell strainer. The strainer was washed with single-cell suspension buffer (SCSB, 2% FCS and 1 mM EDTA in PBS), and the process was repeated until no more red tissue was visible in the strainer. The cells were pelleted at 300 rcf and 4°C for 10 min, the supernatant was discarded, and the cells were resuspended in 2 mL ACK lysis buffer (Thermo Fisher Scientific) per spleen, to remove red blood cells. After 5 min in the lysis buffer, cold PBS was added until 40 mL and the cells were pelleted at 500 rcf and 4°C for 5 min. The supernatant was discarded, and the cells were resuspended in SCSB and passed over a 40 μm cell strainer. The cells were pelleted at 300 rcf and 4°C for 10 min, the supernatant was discarded, and the cells were resuspended in splenocyte medium (RPMI 1640 culture medium (Capricorn Scientific, #RPMI-HXA) supplemented with 10% FCS, GlutaMAX (2 mM), penicillin (100 I.U./mL), streptomycin (50 μg/mL), and 2-mercaptoethanol (50 μM)). The cells were counted using a haemocytometer before seeding. For experiments using solely unstimulated splenocytes, the cells were seeded directly for the respective experiments (see below).

For experiments using both stimulated and unstimulated splenocytes, half the wells of a Nunc™-treated 6-well plate (Thermo Fisher Scientific) were coated with Ultra-

LEAF purified anti-mouse CD3ε antibody (BioLegend, 5 µg/mL) in sterile PBS for 2 h at 37°C. After 2 h the antibody was removed, and 15x10^6 cells were seeded per well in 5 mL complete splenocyte medium supplemented with Ultra-LEAF purified anti-mouse CD28 antibody (BioLegend, 3 µg/mL) and recombinant murine IL2 (PeproTech, 10 U/mL). For unstimulated control cells, 15x10^6 cells were seeded per well in 5 mL complete splenocyte medium supplemented with recombinant murine IL2 (PeproTech, 10 U/mL). All cells were incubated at 37°C, 5% CO_2 overnight. The next day, the activated and naïve cells were scraped, combined in separate tubes and centrifuged at 300 rcf for 10 min. The cells were resuspended in fresh splenocyte medium before being counted using a haemocytometer and seeded for experiments (see below).

Cell sorting of naïve splenocytes for proteomics and Seahorse analysis. Three spleens were harvested, and splenocytes were isolated (as described above) to yield ~400-500x10^6 unstimulated cells. These cells were seeded evenly over the wells of three Nunc™-treated 6-well plates (Thermo Fisher Scientific) in 2 mL fresh splenocyte medium per well. To each well, 2 mL sterculic acid (200 µM) in splenocyte medium was added, to give a final sterculic acid-concentration of 100 µM. The cells were incubated at 37°C, 5% CO_2 for 15 min, to allow for uptake of the fatty acid. All wells were harvested, combined in 50 mL tubes, and washed with fresh medium (x1) and PBS (x1). Each washing step consisted of spinning down (300 rcf, 5 min), aspirating supernatant, and resuspending in wash solution. After the last wash, the cells were resuspended in PBS supplemented with fluorophore **7** (1 µM) and incubated on ice for 35 min, to allow the fluorophore to react with sterculic acid. The cells were washed with cold PBS (x2), where each washing step consisted of spinning down (300 rcf, 5 min, 4°C), aspirating supernatant, and resuspending in wash solution. To perform a viability staining, the cells were resuspended in 750 µL of HBSS (Gibco, #14025092) supplemented with Zombie NIR (BioLegend, #423105, 1:500) and DNase I (Thermo Fisher Scientific, #90083, 30 U/mL), and incubated at RT for 15 min. The rest of the antibody cocktail was diluted in 250 µL HBSS and added to the cells to give a final volume of 1 mL. The following antibodies and dilutions (calculated with 1 mL final volume) were used: PE/Dazzle 594 anti-mouse CD3 (1:800), APC anti-mouse CD4 (1:400), eFluor450 anti-mouse CD44 (1:200), and PE-Cyanine7 anti-mouse CD62L (1:1000). The cells were incubated at RT for an additional 25 min, before addition of 10 mL FACS buffer (PBS with 0.2% BSA and 2 mM EDTA) and centrifugation at 300 rcf, 5 min. The cells were then washed with FACS buffer (x2), before being resuspended in ~1.5 mL FACS buffer. The samples were transported on ice and sorted using a BD FACS Aria III 4L (BD Biosciences, San Jose, CA, USA), following the gating strategy shown in Figure S1A. The experiment was repeated minimum as biological triplicates.

Cell sorting of activated splenocytes for proteomics and Seahorse analysis. Three spleens were harvested, and splenocytes were isolated and activated (as described previously). Subsequently, the same protocol as for sorting naïve splenocytes (described above) was used, except for the PE/Dazzle 594 anti-mouse CD3 antibody which was diluted at 1:200 instead of 1:800. The FACS gating strategy is shown in Figure S1B. The experiment was repeated as biological triplicates.

Seahorse analysis. 1-2x10^6 sorted low- and high-uptake cells were used to perform the Seahorse Real-Time ATP Rate Assay. Inhibitors and uncouplers were prepared in XF assay media, supplemented with 5 mM D-(+)-glucose for sequential addition at the appropriate final concentrations of oligomycin A (1.8 µM), and antimycin A (2 µM) (all Sigma-Aldrich). Cells were placed in a non-CO2 incubator at 37°C for 1 h prior to the assay. Basal respiration (OCR) and extracellular acidification rate (ECAR) were measured by the Seahorse Biosciences XFe24 Extracellular Flux Analyser (Agilent Technologies, Santa Clara, CA, USA). Oxygen consumption rates (OCR) and ECAR were measured and analysed using the Agilent online analysis tool. Values recorded were normalised to cell numbers seeded. Baseline readings were established, and the effects of specific inhibitors and uncouplers on OCR and ECAR were assessed using repeated measures ANOVA and plotted as bar charts, and scatter plots. Error bars indicating standard deviation were included to illustrate variability within the data.

Preparation of sorted samples for proteomics. From the sorted cells (described above), $2x10^5$ cells of each population were taken for total-digest proteomics. The samples were spun down at 300 rcf, 5 min, 4°C, and the supernatant was aspirated. The cell pellets were plunge frozen and stored at -80°C until further processing. Upon thawing of the samples, they were resuspended in 15 µL lysis buffer (250 mM sucrose, 5 mM EDTA, 1x cOmplete™ protease inhibitor (Roche) in PBS). The samples were lysed by sonication (Qsonica Q700 Microplate Sonicator, 4x10 s pulses, 10% amplitude, 0°C). Protein concentration was measured by Qubit Protein assay (Invitrogen) according to the manufacturer's protocol, and all samples were found to contain ~4 µg of protein. The proteins were precipitated by adding 500 µL cold (-80°C) acetone, vortexing, and incubating the samples at -80°C for 1 h. The samples were spun down at 20 000 rcf, 15 min, 4°C, and the supernatant was poured off. To wash, 300 µL acetone was added to each sample, followed by vortexing and sonication (2x10 s pulses, 10% amplitude, 0°C). The samples were incubated at -80°C overnight, before being spun down at 20 000 rcf, 15 min, 4°C. The supernatant was poured off, and the samples were airdried for 2 min to ensure all the acetone had evaporated. To redissolve and denature the proteins, 20 µL urea (8 M) in NH_4HCO_3 (100 mM), pH 8 was added, and the samples were shaken for 30 min at 37°C, 1000 rpm. The proteins were then reduced by addition of dithiothreitol (DTT, 5 mM) and the samples were shaken for 15 min at 65°C, 800 rpm. The samples were cooled down before addition of iodoacetamide (IAA, 10 mM) and incubation for 30 min at RT in the dark, to acetylate all proteins. Unreacted IAA was quenched by addition of DTT (7 mM). All samples were diluted with 170 µL $CaCl_2$ (1 mM) in NH_4HCO_3 (20 mM) to ensure urea concentrations <1 M. All samples were transferred to Protein LoBind tubes (Eppendorf), and sequencing-grade trypsin (Promega, 0.2 µg) was added. The trypsin digestion mixture was shaken at 37°C, 1000 rpm overnight, before being quenched by addition of 5 µL 50% trifluoroacetic acid (TFA) in MilliQ. Peptides were desalted using Empore™ C18 StageTips (CDS Analytical) preconditioned with 50 µL MeOH, 50 µL of 0.05% (v/v) TFA in 60% (v/v) acetonitrile/MilliQ (solution B) and 50 µL 0.05% (v/v) TFA in MilliQ (solution A) by centrifugation (600 rcf, 2 min). The peptides were washed with solution A (100 µL, 800 rcf, 3 min) and eluted into new Protein LoBind tubes using solution B (100 µL, 800 rcf, 3 min). The samples were concentrated using an Eppendorf SpeedVac (Eppendorf Concentrator Plus 5301 or 5305) and stored at -80°C until measurement. Upon measurement, desalted peptide samples were reconstituted in 40 µL LC-MS solution (97:3:0.05 MilliQ, acetonitrile, TFA).

LC-MS/MS measurements. Peptides (prepared as described above) were separated via nanoflow reversed-phase liquid chromatography using a nanoElute 2 LC system (Bruker Daltonics) coupled to a timsTOF HT mass spectrometer (Bruker) with 0.1% FA (solution A) and 0.1% FA/99.9% ACN (solution B) as the mobile phases. The samples were loaded on a trap column (PepMap C18, 5 mm x 0.3 mm, 5 µm, 100 Å, Thermo Scientific) followed by elution and separation on the analytical column (PepSep C18, 25 cm x 75 µm, 1.5 µm, 100 Å, Bruker) kept at 50 °C using a gradient of 2 - 25% solvent B in 25 min, 25 - 32% B in 5 min, 32 - 95% B in 5 min and 95% B for 10 min at a flow rate of 300 nL/min. Peptides were introduced to a TimsTOF HT (Bruker Daltonics) using a 20 µm ID fused silica emitter (Bruker Daltonics) installed in a nano-electrospray ion source (CaptiveSpray source, Bruker Daltonics) with spray voltage set to 1500 V.

For DIA acquisition, peptides were analysed with a TimsTOF HT (Bruker Daltonics) running in DIA-PASEF mode. The DIA-PASEF method was optimized for the specific sample type using the py_diAID tool.[110] The method covered an ion mobility range from 1.35 to 0.7 Vs cm-2 and an m/z range of 300 to 1300, using 10 DIA-PASEF scans with two isolation windows per scan, resulting in a cycle time of 1.1 s. Collision energy was linearly decreased from 59 eV at 1.6 Vs cm-2 to 20 eV at 0.6 Vs cm-2. For all experiments the ion mobility dimension was calibrated linearly using three selected ions of the Agilent ESI LC/MS Tuning Mix [m/z, 1/K0: (322.0481, 0.7318 Vs cm−2), (622.0289, 0.9848 Vs cm−2), (922.0097, 1.1895 Vs cm−2)]. Mass calibration was performed with sodium formate in HPC mode.

Proteomics data analysis. The raw files were analysed using DIA-NN (version 1.8.1). Searches were performed against a UniProt database of the mouse proteome (UPID: UP000000589, downloaded 17th March 2024).[42] The output file "report.unique_genes_matrix.tsv" from DIA-NN was used for further analysis in R Statistical Software.[31] At most 1 missing value in either the low- or high-uptake samples were allowed, and missing values were imputed with the average value of the remaining measurements. In cases where all values were missing from either the low- or high-uptake samples, the missing values were imputed with a negligible small number to allow for further processing and statistical calculations. Significantly differentially expressed proteins were determined using the empirical Bayes method in the Limma package[111] (Version 3.58.1) in R, and the significant proteins were determined to have a 2-fold difference between the expression levels of low- and high-uptake samples with an adjusted p-value of <0.05. Pathway analysis was performed using the clusterProfiler package in R.[43]

Checking integrity of RNA by 1% agarose gel after click reactions. $1x10^6$ DC2.4 cells were seeded per well in 6-well plates, and incubated at 37°C, 5% CO_2 overnight to allow the cells to attach. The samples shown in Figures S2A & S2B were treated with either sterculic acid (50 µM), oleic acid-alkyne (50 µM), oleic acid-azide (50 µM) or DMSO-vehicle (0.5%) in fresh DC2.4 medium for 1 h at 37°C, 5% CO_2, followed by a wash with DC2.4 medium x1 and PBS x1. The samples shown as "Live" in Figure S2A were reacted with fluorophore **7** (5 µM) or DMSO vehicle (0.25%) in fresh DC2.4 medium for 1 h at 37°C, 5% CO_2. The medium was aspirated and the cells were resuspended in 500 µL TRIzol reagent (Invitrogen) per well, before being transferred to 1.5 mL Eppendorf tubes. The samples were plunge frozen in liquid nitrogen and stored at -80°C until further processing. Simultaneously, the samples shown as

“Fixed” in Figures S2A & S2B were fixed with 4% PFA in PBS for 15 min at RT. The fixed cells were washed with PBS x2, and permeabilised with PBS supplemented with saponin (0.1%) and RNase inhibitor (40 U/mL). After permeabilization, the cells were again washed with PBS x2, followed by click reaction with complete IEDDA cocktail, complete CuAAC cocktail, or DMSO vehicle (0.25%) in PBS for 1 h at RT in the dark. The IEDDA cocktail consisted of fluorophore **7** (5 µM) in PBS. The complete CuAAC cocktail consisted of $CuSO_4$ (1 mM), sodium ascorbate (10 mM), THPTA ligand (1 mM), amino-guanidine (10 mM), HEPES pH 7.2 (100 mM), and AZDye 488 alkyne/azide (5 µM). The fixed cells were then washed with PBS x2, before addition of 500 µL TRIzol reagent (Invitrogen) per well. The fixed cells were scraped to loosen them from the plate and transferred to 1.5 mL Eppendorf tubes. To all the fixed samples, proteinase K (40 U/mL, New England Biolabs, #P8197S) was added, and the samples were incubated at 56°C for 1 h, followed by 10 min at RT and 5 min on ice. All fixed cell samples were plunge frozen in liquid nitrogen and stored at -80°C until further processing.

For the samples shown in Figure S2C, a similar protocol was followed as described above. The only differences were that there was no oleic acid analogues added to these samples, and the separate components of the CuAAC cocktail (diluted in 100 mM HEPES, pH 7.2) were also added to the cells.

All the prepared samples were thawed, 100 µL chloroform was added to each, and they were vortexed vigorously for 15 s. After centrifugation at 20 000 rcf for 5 min, the supernatant (aqueous phase, ~200 µL) was transferred to new tubes. To the new tubes, 100 µL chloroform was added, they were vortexed vigorously, and spun down at 20 000 rcf for 5 min. The supernatant (~180 µL) was transferred to new tubes, 180 µL isopropanol was added, and the samples were vortexed. RNA precipitation occurred by incubating the samples for 20 min at RT, followed by centrifugation at 20 000 rcf for 15 min. The pellets were washed twice with ethanol (70%), and airdried for 5 min. RNA isolated from live cells was reconstituted in 15 µL MilliQ, whereas RNA from fixed cells was reconstituted in 10 µL MilliQ. The RNA concentration was measured with a DeNovix DS-11 spectrophotometer, and 1 µg RNA from each sample was mixed with RNA loading dye (Thermo Fisher Scientific, #R0641, 1x) supplemented with GelRed and loaded on 1% agarose gels in TAE buffer. As a reference, RiboRuler High Range RNA ladder (Thermo Fisher Scientific, #SM1821) was also added to the gels. The gels were run at 80 V for 45 min and were imaged on a Chemidoc MP imaging system (Bio-Rad).

Cell sorting of splenocytes for single-cell RNA sequencing. One spleen was harvested, and the splenocytes were isolated and stimulated as described above. The stimulated cells were scraped from the 6-well plate and counted using a haemocytometer. $8x10^6$ cells were seeded in 800 µL splenocyte medium in one well of an uncoated 12-well plate. To the same well, 800 µL sterculic acid (50 µM) in splenocyte medium was added, to give a final sterculic acid-concentration of 25 µM. The cells were incubated at 37°C, 5% CO_2 for 1 h, to allow for uptake of the fatty acid. The cells were harvested, transferred to a 15 mL tube, and washed with fresh medium (x2). Each washing step consisted of spinning down (300 rcf, 5 min), aspirating supernatant, and resuspending in wash solution. The cells were resuspended in 1.6 mL fresh medium supplemented with fluorophore **7** (1 µM) and seeded in a well in an uncoated 12-well plate. The cells were incubated at 37°C, 5%

CO_2 for 1 h, to allow the fluorophore to react with sterculic acid, followed by being harvested, transferred to a 15 mL tube, and washed with fresh medium (x1) and PBS (x1). To perform a viability staining, the cells were resuspended in 1 mL Zombie NIR (1:1000) in PBS, and incubated at RT for 20 min. After staining, two washing steps with fresh medium (x1) and PBS (x1) were performed. The cells were fixed with 2% paraformaldehyde (PFA) in PBS for 30 min, before unreacted PFA was quenched with PBS supplemented with glycine (20 mM) and RNase inhibitor (40 U/mL). A last wash with FACS buffer was performed, before the cells were resuspended in 600 µL FACS buffer supplemented with RNase inhibitor (40 U/mL). The samples were transported on ice and sorted using a BD FACS Aria III 4L (BD Biosciences, San Jose, CA, USA), according to the gating strategy shown in Figure S3.

scRNAseq workflow & data analysis. $4x10^5$ cells of the low and high StA-uptake populations were collected by FACS (as described above) and were handed over to the Leiden Genome Technology Centre (LGTC) for processing, measurement, and data analysis. The samples were analysed using the Chromium Fixed RNA Kit (10x Genomics).

Supplementary Figures & Tables

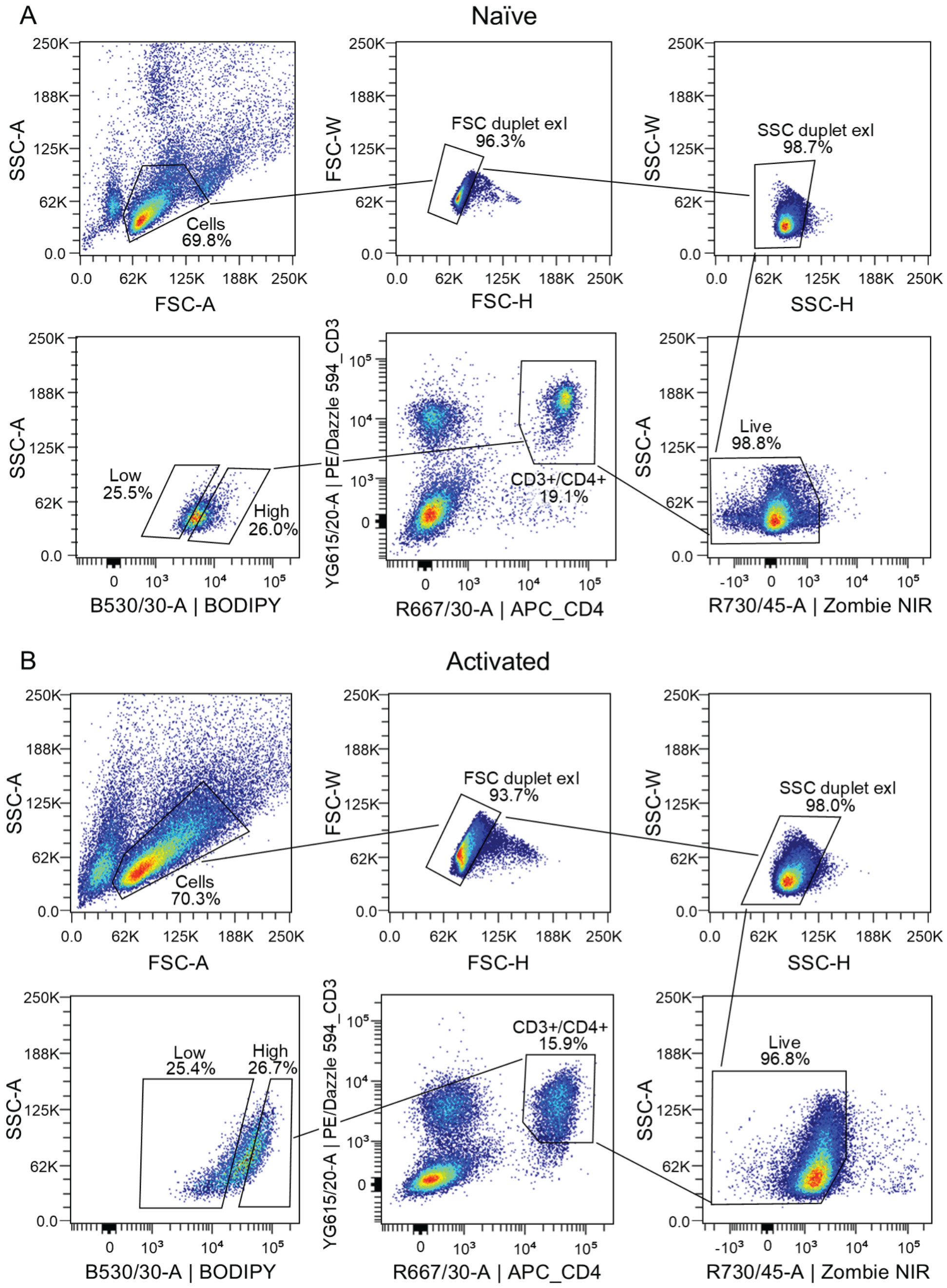

Figure S1: *Example of FACS gating strategy for proteomics and Seahorse analysis of* ***A)*** *naïve splenocytes,* ***B)*** *αCD3/αCD28-activated splenocytes.*

Table S1: *List of significantly up- and downregulated proteins (in the high-uptake population) after proteomics analysis of naïve CD3+/CD4+ T cells upon high or low uptake of StA.*

Upregulated	Downregulated
Cd74	Fbxo7
Ncapg	
Ncapd2	
Cdk1	
Ncaph	
Kif2c	
Swap70	
Pygm	
Kif4	
Pld4	
Incenp	
Tbc1d4	
Supt20h	
Mafg	
Dut	
Rbfa	
Top2a	
Marcksl1	
Stmn1	
Smc2	
Anxa2	
Dhfr	

Table S2: *List of significantly up- and downregulated proteins (in the high-uptake population) after proteomics analysis of αCD3/αCD28-activated CD3+/CD4+ T cells upon high or low uptake of StA. The table continues on the next page.*

Upregulated			**Downregulated**		
Mapkapk5	Dut	Rps25	Fbxl22	Plp2	Tra2b
Smad4	Btf3	Ipo5	Irf1	H1-5	Dok2
Mtg2	Psat1	Pdcd2	Rnf13	Cd3d	Atp2a1
Tsnaxip1	Srm	Shmt2	Ifngr1	Pecam1	Kdsr
Kcna6	Rps17	Ddx3x	Depdc1b	S100a6	Tmub1
Heatr9	Cdca7	Acaca	Pkp1	Anxa1	Krt17
Maff	Gpatch4	Nudt5	Endod1	Gimap3	Nqo2
Cops7a	Impdh2	Noc2l	Ifit1bl1	Phf11b	Cap2
Fem1aa	Rpl22	Rps11	Frmd4b	Cox6c	Fam98c
Zc3h7b	Stard4	Aimp2	Krt4	Ahnak	Syne3
Uqcc6	Ifrd2	Hells	Adap1	Trafd1	Tiam1
Ccdc97	Cyp51a1	Grwd1	Tmem71	Prkab1	Eeig1
Nexmif	Rps3	Gemin8	H2-DMb2	Cnst	Cd247
Akirin2	Smyd5	Surf2	Mbtd1	Hide1	Rasa3
Zeb1	Znhit3	Aprt	Trbv19	Cd48	Slc28a2
Smg7	Colgalt1	Acly	Ifit2	Fgd3	Tgm2
Klhl9	Nolc1	Dph6	Ecm1	Sp100	Hmgn1
Ctnna1	Hk2	Rrp15	Cdkn1b	Dsp	Ets1
Dhrs11	Fdps		Prss59	Aldh3a2	Dop1b
Aasdhppt	Snrpb		Oasl2	H2bc14	Hsdl2
Pprc1	Fasn		S100a4	Iigp1	Znf710
Trim26	Larp4		Vmn2r3	Tmem245	H2bc3
Pmf1	Spin4		Cep76	Cybc1	Tm9sf3
Crcp	Eif4a1		Ing1	Chdh	Cyria
Sar1b	Rpsa		Krt76	Kif1b	Vps13c
Ccdc127	Eif4e2		Cd3e	H2-M3	Nfatc2ip
Polr2d	Nob1		Lamtor5	Hist1h2bp	Arl6ip4
Tatdn2	Abcf2		Sell	Il4r	Itgb3
Lhpp	Psmg4		Cirbp	Fbxo6	Trbv1
Gga2	Hspbp1		Rtp4	Cd47	Elmo2
Crabp2	Gzmb		Slfn5	Trim14	Tdrp
Arl1	Dohh		Pdcd4	S100a11	Kctd12
Snapc1	Heatr3		Hba	Ubac2	H2ax

Upregulated (cont.)		**Downregulated** (cont.)		
Atf6	Hat1	Dapl1	Krt5	Elf1
Nedd9	Aven	Try10	Sipa1l1	Dennd1c
Gal3st4	Mrto4	Krt16	Mdm1	Creb1
Ogfod1	Cluh	Nucks1	Saraf	Sigirr
Bcat1	Pcna	Dpys	Cmc2	Rcsd1
Hmgcs1	Mtrr	Ifit1	Cytip	Cd84
Kpna2	Ppat	Krt42	Zbtb2	As3mt
Eif5a	Acbd6	H2bc26	Irf7	Map3k3
Lss	Rpap2	S100a13	Ifi203	Sfxn3
Znhit6	Znrd2	Ighg1	Itm2b	Galm
Znf583	Ltv1	Sun2	Sh3bgrl	Zbp1
Ntmt1	Fam98a	Ltb	Amacr	Ccdc71
Ybx3	Mthfd2	Casp1	Tma7	Gvin1
Psmb5	Rps24	Clec2d	Mndal	Itgb7
Rpl22l1	Rps23	H1-2	Cd3g	Anxa5
Cdc45	Dtd2	Trp53i11	Alb	Gbp7
Psmg3	Orc6	Ms4a6b	Bles03	Fchsd1
Slfn2	Nufip1	Epsti1	H1-0	Plgrkt
Dnajc15	Edrf1	Ifi204	Anxa2	Ddah2
Eef1akmt4	Acsl4	Inppl1	Znf551	Col4a2
Fpgs	Naa50	Cd74	Cmpk2	Rab22a
Pmvk	Cdc123	H1-1	Cstb	Tmx4
Idi1	Rpl35	Tbc1d8b	Vkorc1	Fam3c
Mak16	Rplp0	Abcg3	Arid5a	Coq9
Etf1	Ipo4	Ephx1	Atp2a3	Myo15a
Nap1l1	Hypk	Hist2h2bb	Cfap20	Zfp512b
Uck2	Ubap2	Abraxas1	Lmna	Smarca2
Pabpc4	Cks2	Gimap1	Srsf2	Hmgb2
Ttc27	Irf4	H2bu2	Sting1	Esyt2
Rpl30	C1d	Adgre5	Gsn	Gbp9
Gxylt1	Pwp1	Stat2	Capg	Rnf169
Mcm10	Rps12	Krt12	Pafah1b3	Arhgef18
Pla2g12a	Serpinb6b	Ctse	Msh3	Hsd11b1
Aen	Umps	Ptms	Sit1	Igtp
Cars1	Blm	Srd5a3	Zfp362	Hp1bp3

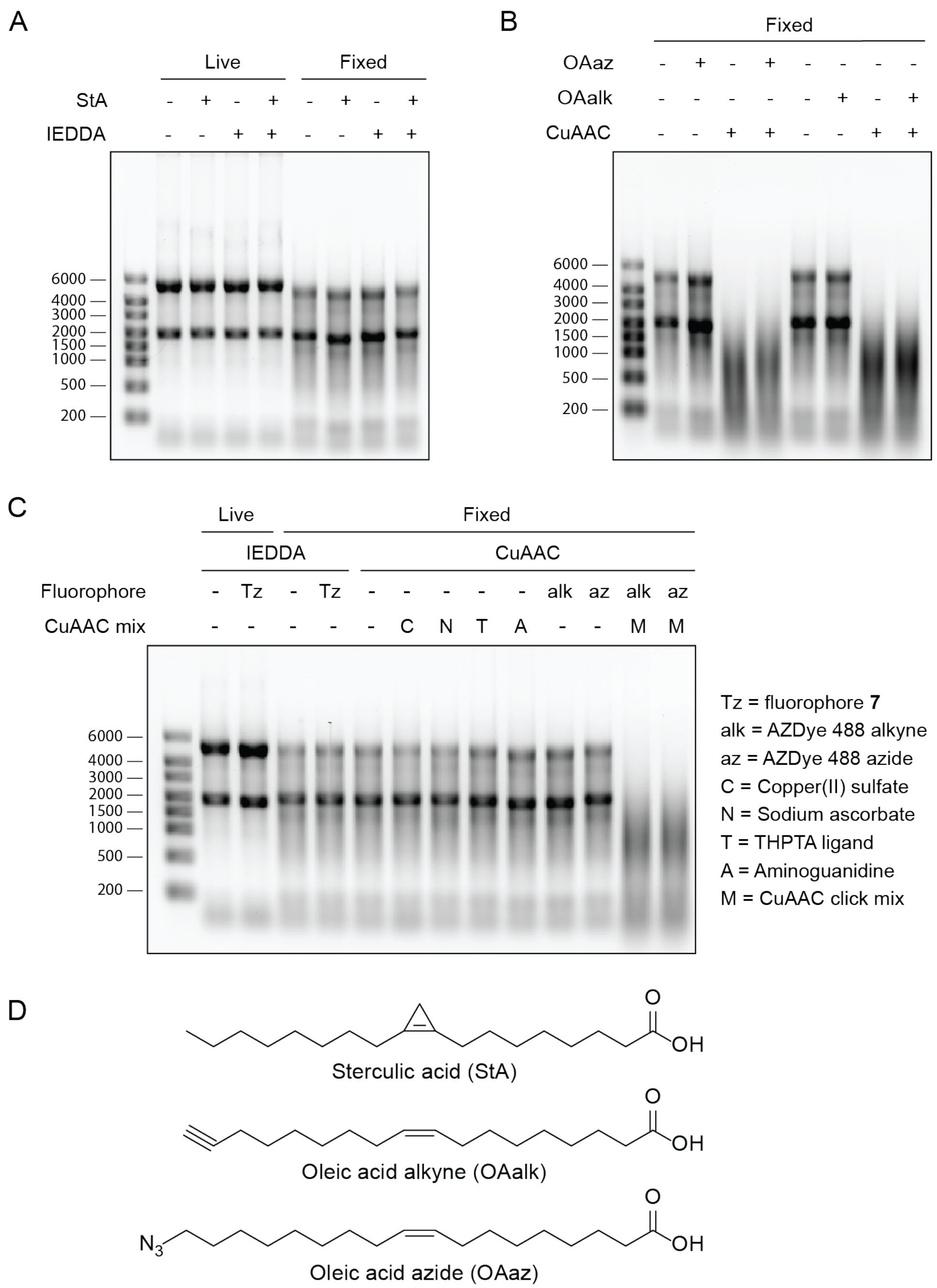

Tz = fluorophore **7**
alk = AZDye 488 alkyne
az = AZDye 488 azide
C = Copper(II) sulfate
N = Sodium ascorbate
T = THPTA ligand
A = Aminoguanidine
M = CuAAC click mix

Figure S2: *RNA gels showing intact RNA after IEDDA, but not after CuAAC.* ***A)*** *IEDDA in live and fixed cells.* ***B)*** *CuAAC in fixed cells.* ***C)*** *IEDDA and CuAAC with each individual click mix component.* ***D)*** *Structures of oleic acid analogues with cyclopropene (sterculic acid, StA), alkyne (oleic acid alkyne, OAalk) and azide (oleic acid azide, OAaz) click handles.*

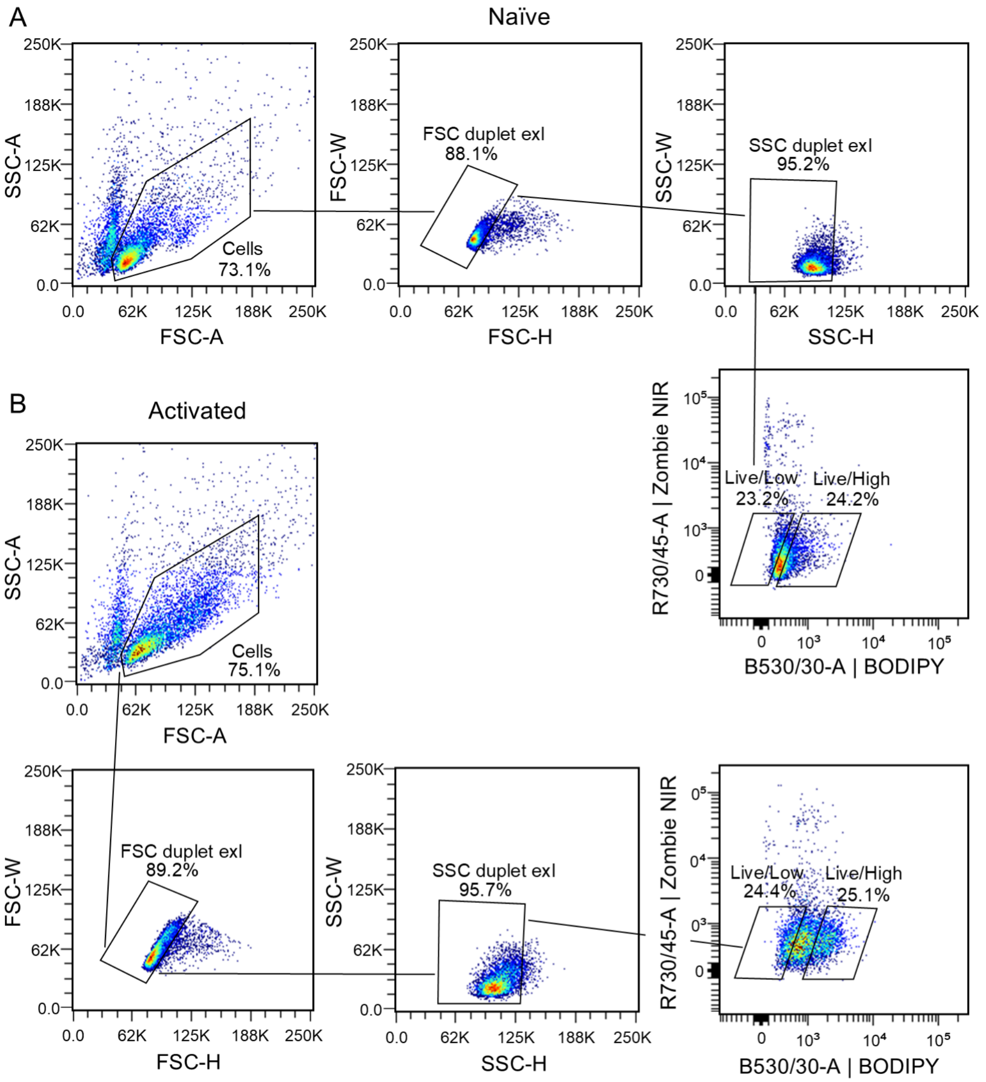

Figure S3: *Example of FACS gating strategy for scRNAseq of* ***A)*** *naïve splenocytes,* ***B)*** *αCD3/αCD28-activated splenocytes.*

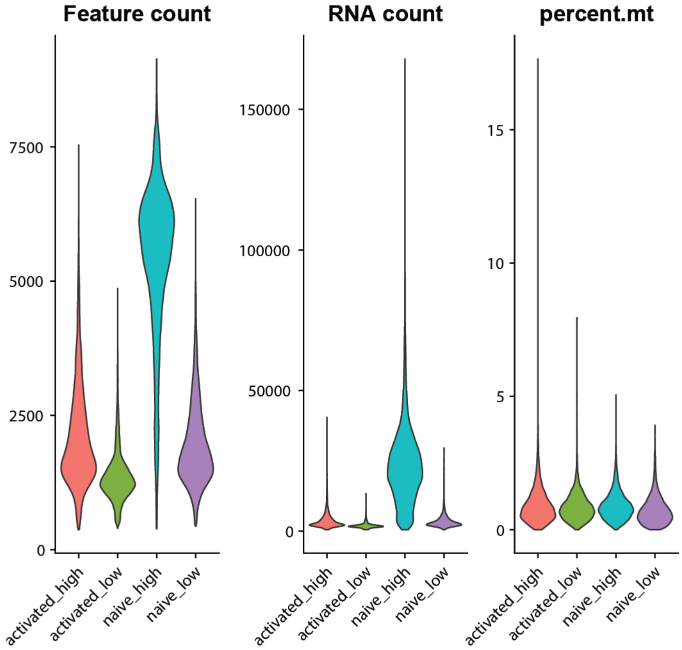

Figure S4: *Quality control analysis of all samples submitted for scRNAseq showing that the high-uptake sample of naïve splenocytes is quite different from the other samples. It contains more feature and RNA counts than the other samples.*

Table S3: *Immune cell subsets corresponding to clusters identified from the scRNAseq analysis (from Figure 2). The immune cell subsets were determined based on expression of relevant marker genes from the scRNAseq data.*

Cluster	Immune subset	Relevant marker genes
0	CD4+ T cells	*CD3E, CD3D, CD3G, CD3Z, CD4*
1	CD8+ T cells	*CD3Z, CD8A, CD8B1*
2	B cells	*CD19, IGHM, IGHD, IGHE*
3	B cells	*CD19, IGHM, IGHD, IGHE*
4	B cells	*CD19, IGHM, IGHD, IGHE*
5	NK cells	*CD16, CD27, CD161, KLRK1, NCR1*
6	B cells	*CD19, IGHM, IGHD, IGHE, IGHG*
7	Mixed (T & B cells)	*CD3Z, CD4, CD8B1, CD19, IGHD, IGHE*
8	CD8+ T cells	*CD3Z, CD8A, CD8B1*
9	CD8+ T cells	*CD3Z, CD8A, CD8B1*
10	B cells	*CD19, IGHM, IGHD, IGHE*
11	B cells	*CD19, IGHM, IGHG*
12	CD8+ NKT cells	*CD3Z, CD8A, CD16, CD161, CD122, KLRK1*
13	CD4+ NKT cells	*CD3Z, CD4, CD161, CD122, KLRK1, NCR1*
14	CD4+ Treg	*CD3Z, CD4, FOXP3*
15	Monocytes	*CD68, CD172A, CD86, CD40, CD80*
16	CD8+ T cells	*CD8A, CD8B1*
17	Mixed	*CD8A, CD8B1, CD161, CD122, KLRK1, NCR1*
18	CD4+ T cells	*CD3Z, CD4*
19	Monocytes	*CD11B, CD14, CD16, CD68, CD172A, CD40, CD80*
20	Mixed	*CD3Z, CD4, CD8A, CD8B1*
21	Monocytes	*CD11B, CD14, CD16, CD172A, CD80*
22	NK cells	*CD56, CD49B*
23	Monocytes	*CD68, CD172A*

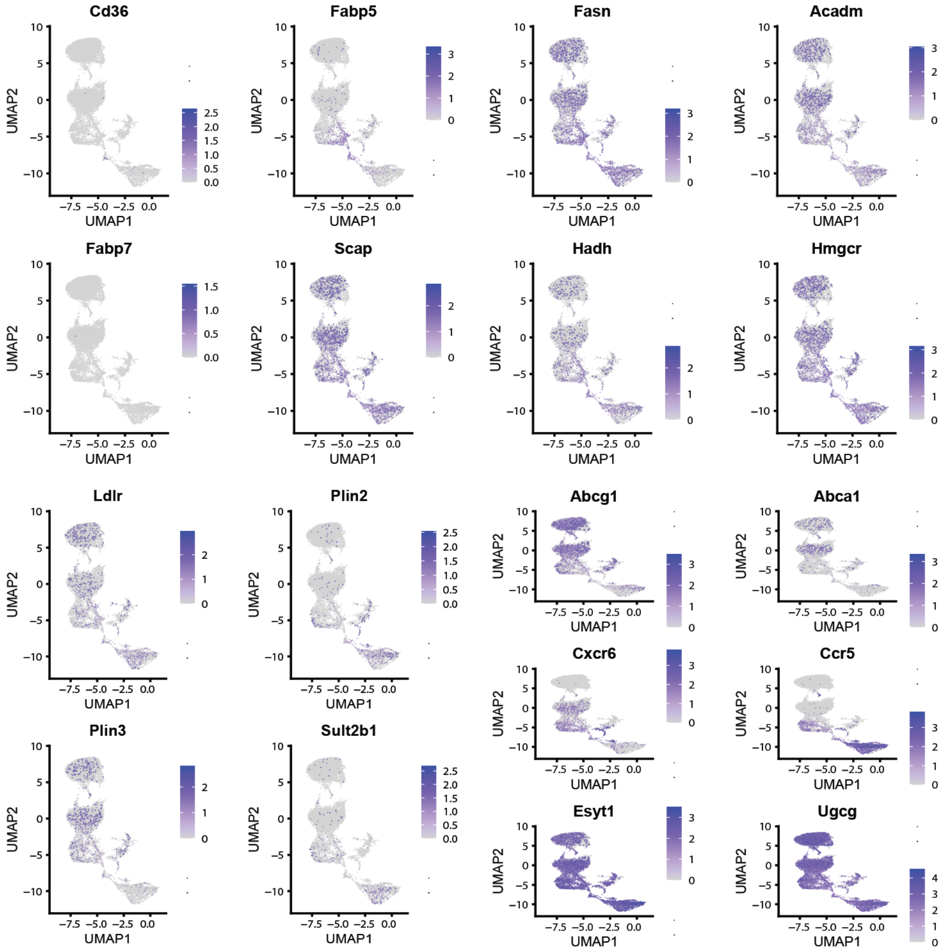

Figure S5: *Gene expression distribution from scRNAseq of genes related to lipid metabolism. The expression distribution is highlighted in clusters containing all T, NKT, and NK cells.*

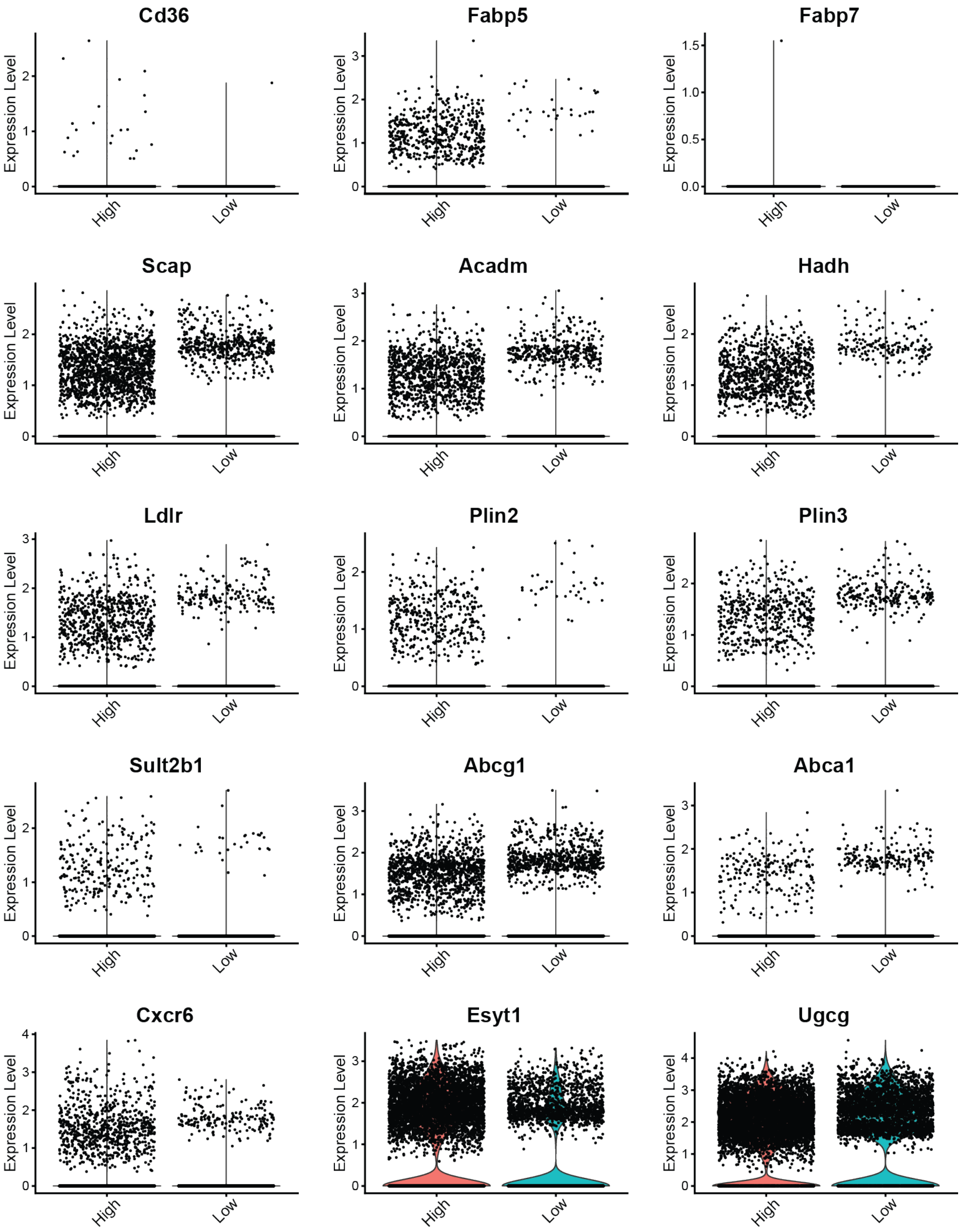

__Figure S6:__ Expression of genes related to lipid metabolism from scRNAseq in the high- and low-uptake populations of T, NKT, and NK cells, represented as violin plots.

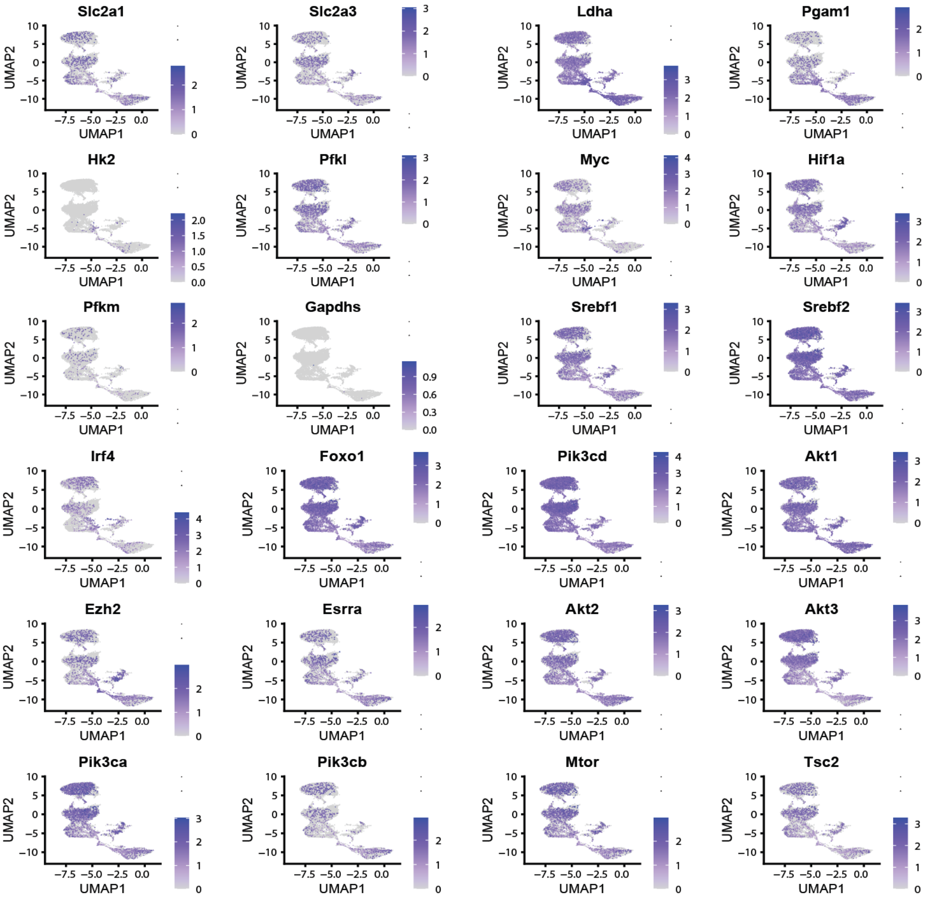

Figure S7: *Gene expression distribution from scRNAseq of genes related to glycolysis and glucose metabolism. The expression distribution is highlighted in clusters containing all T, NKT, and NK cells.*

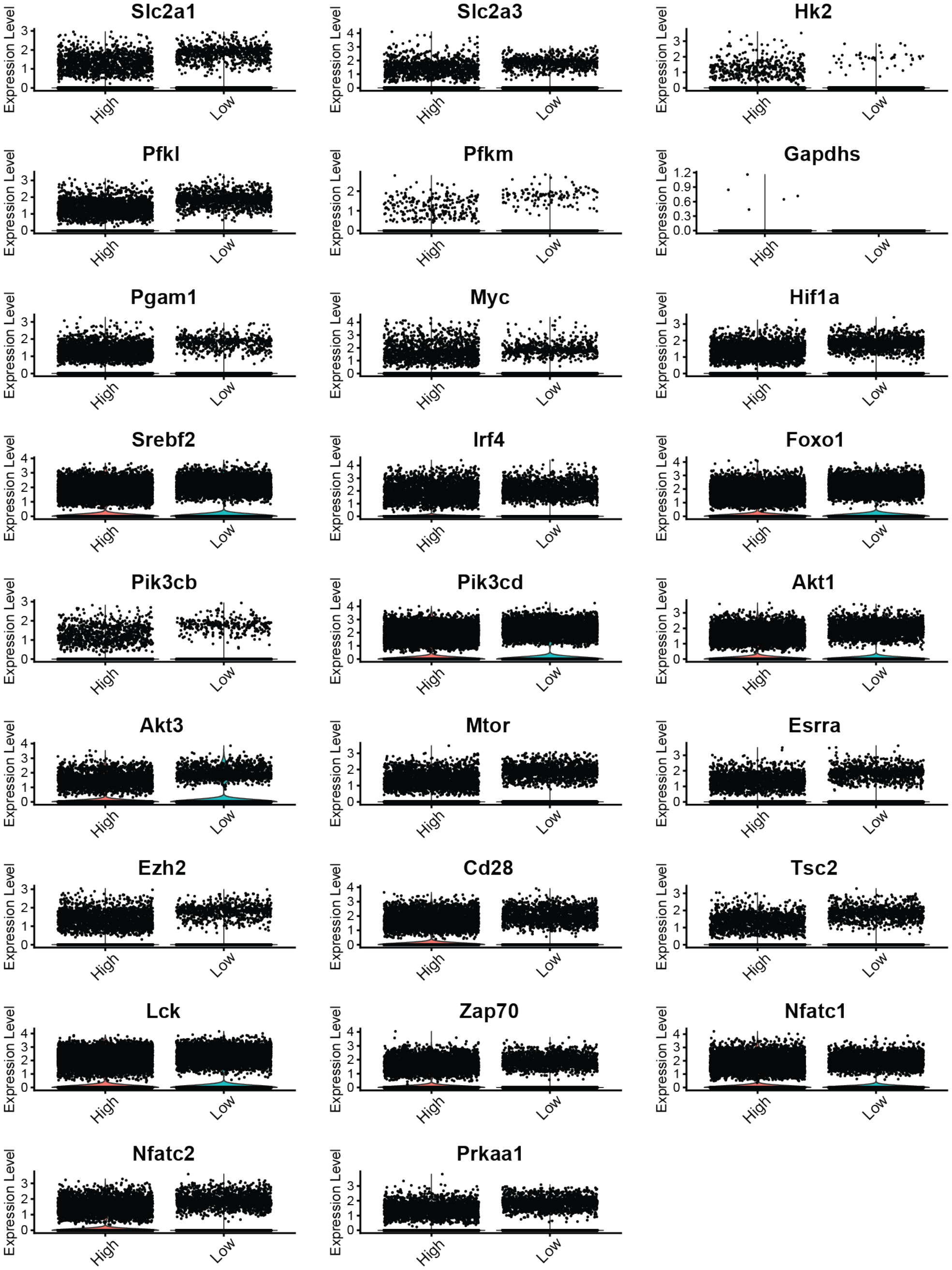

__Figure S8:__ Expression of genes related to glycolysis and glucose metabolism from scRNAseq in the high- and low-uptake populations of T, NKT, and NK cells, represented as violin plots.

References

1. Fox, C. J., Hammerman, P. S. & Thompson, C. B. Fuel feeds function: energy metabolism and the T-cell response. *Nature Reviews Immunology* **5**, 844–852 (2005).
2. MacIver, N. J., Michalek, R. D. & Rathmell, J. C. Metabolic Regulation of T Lymphocytes. *Annu Rev Immunol* **31**, 259–293 (2013).
3. Buck, M. D., O'Sullivan, D. & Pearce, E. L. T cell metabolism drives immunity. *Journal of Experimental Medicine* **212**, 1345–1360 (2015).
4. Jacobs, S. R. *et al.* Glucose Uptake Is Limiting in T Cell Activation and Requires CD28-Mediated Akt-Dependent and Independent Pathways. *The Journal of Immunology* **180**, 4476–4486 (2008).
5. Geiger, R. *et al.* L-Arginine Modulates T Cell Metabolism and Enhances Survival and Anti-Tumor Activity. *Cell* **167**, 829–842 (2016).
6. Angela, M. *et al.* Fatty acid metabolic reprogramming via mTOR-mediated inductions of PPARγ directs early activation of T cells. *Nat Commun* **7**, (2016).
7. Pan, Y. *et al.* Survival of tissue-resident memory T cells requires exogenous lipid uptake and metabolism. *Nature* **543**, 252–256 (2017).
8. Kidani, Y. *et al.* Sterol regulatory element–binding proteins are essential for the metabolic programming of effector T cells and adaptive immunity. *Nat Immunol* **14**, 489–499 (2013).
9. Gorjão, R., Cury-Boaventura, M. F., de Lima, T. M. & Curi, R. Regulation of human lymphocyte proliferation by fatty acids. *Cell Biochem Funct* **25**, 305–315 (2007).
10. Passos, M. E. P. *et al.* Differential effects of palmitoleic acid on human lymphocyte proliferation and function. *Lipids Health Dis* **15**, 217 (2016).
11. von Hegedus, J. H. *et al.* Oleic acid enhances proliferation and calcium mobilization of CD3/CD28 activated CD4+ T cells through incorporation into membrane lipids. *Eur J Immunol* **54**, (2024).
12. Miura, S. *et al.* Increased proliferative response of lymphocytes from intestinal lymph during long chain fatty acid absorption. *Immunology* **78**, 142–146 (1993).
13. Ioan-Facsinay, A. *et al.* Adipocyte-derived lipids modulate CD4+ T-cell function. *Eur J Immunol* **43**, 1578–1587 (2013).
14. Zhu, Y. *et al.* Oleic acid causes apoptosis and dephosphorylates Bad. *Neurochem Int* **46**, 127–135 (2005).
15. Reilly, N. A. *et al.* Oleic acid triggers metabolic rewiring of T cells poising them for T helper 9 differentiation. *iScience* **27**, (2024).
16. Hensel, J. A., Khattar, V., Ashton, R. & Ponnazhagan, S. Characterization of immune cell subtypes in three commonly used mouse strains reveals gender and strain-specific variations. *Laboratory Investigation* **99**, 93–106 (2019).
17. Wang, H. *et al.* Analysis of spleen histopathology, splenocyte composition and haematological parameters in four strains of mice infected with Plasmodium berghei K173. *Malaria Journal* **20**, 249 (2021).
18. Grosjean, C. *et al.* Isolation and enrichment of mouse splenic T cells for ex vivo and in vivo T cell receptor stimulation assays. *STAR Protocols* **2**, 100961 (2021).
19. Riddell, S. R. & Greenberg, P. D. The use of anti-CD3 and anti-CD28 monoclonal antibodies to clone and expand human antigen-specific T cells. *Journal of Immunological Methods* **128**, 189–201 (1990).
20. Schumann, J., Stanko, K., Schliesser, U., Appelt, C. & Sawitzki, B. Differences in CD44

Surface Expression Levels and Function Discriminates IL-17 and IFN-γ Producing Helper T Cells. *PLOS ONE* **10**, (2015).

21. Bajnok, A., Ivanova, M., Rigó Jr., J. & Toldi, G. The Distribution of Activation Markers and Selectins on Peripheral T Lymphocytes in Preeclampsia. *Mediators of Inflammation* **2017**, (2017).
22. Wu, T. *et al.* Cell Granularity Reflects Immune Cell Function and Enables Selection of Lymphocytes with Superior Attributes for Immunotherapy. *Advanced Science* **10**, (2023).
23. Waugh, R. E., Lomakina, E., Amitrano, A. & Kim, M. Activation effects on the physical characteristics of T lymphocytes. *Frontiers in Bioengineering and Biotechnology* **11**, (2023).
24. Pollizzi, K. N., Waickman, A. T., Patel, C. H., Sun, I. H. & Powell, J. D. Cellular Size as a Means of Tracking mTOR Activity and Cell Fate of CD4+ T Cells upon Antigen Recognition. *PLOS ONE* **10**, (2015).
25. Yoo, I., Ahn, I., Lee, J. & Lee, N. Extracellular flux assay (Seahorse assay): Diverse applications in metabolic research across biological disciplines. *Molecules and Cells* **47**, 100095 (2024).
26. Ma, S., Ming, Y., Wu, J. & Cui, G. Cellular metabolism regulates the differentiation and function of T-cell subsets. *Cell Mol Immunol* **21**, 419–435 (2024).
27. Wang, R. & Green, D. R. Metabolic reprogramming and metabolic dependency in T cells. *Immunological Reviews* **249**, 14–26 (2012).
28. Slack, M., Wang, T. & Wang, R. T cell metabolic reprogramming and plasticity. *Molecular Immunology* **68**, 507–512 (2015).
29. Hu, C. *et al.* Immune cell metabolism and metabolic reprogramming. *Molecular Biology Reports* **49**, 9783–9795 (2022).
30. Wright, M. H. & Sieber, S. A. Chemical proteomics approaches for identifying the cellular targets of natural products. *Natural Product Reports* **33**, 681–708 (2016).
31. R Core Team. R: A Language and Environment for Statistical Computing. Preprint at (2023).
32. Diril, M. K. *et al.* Cyclin-dependent kinase 1 (Cdk1) is essential for cell division and suppression of DNA re-replication but not for liver regeneration. *Proceedings of the National Academy of Sciences* **109**, 3826–3831 (2012).
33. Wells, A. D. & Morawski, P. A. New roles for cyclin-dependent kinases in T cell biology: linking cell division and differentiation. *Nature Reviews Immunology* **14**, 261–270 (2014).
34. Schröder, B. The multifaceted roles of the invariant chain CD74 — More than just a chaperone. *Biochimica et Biophysica Acta (BBA) - Molecular Cell Research* **1863**, 1269–1281 (2016).
35. Westmeier, J. *et al.* Macrophage migration inhibitory factor receptor CD74 expression is associated with expansion and differentiation of effector T cells in COVID-19 patients. *Frontiers in Immunology* **14**, (2023).
36. Bonnin, E. *et al.* CD74 supports accumulation and function of regulatory T cells in tumors. *Nature Communications* **15**, 3749 (2024).
37. Zhang, L. *et al.* CD74 is a functional MIF receptor on activated CD4+ T cells. *Cellular and Molecular Life Sciences* **81**, 296 (2024).
38. Zhang, L. *et al.* CD74 is a functional MIF receptor on activated CD4+ T cells. *Cellular and Molecular Life Sciences* **81**, 296 (2024).

39. Bonnin, E. *et al.* CD74 supports accumulation and function of regulatory T cells in tumors. *Nature Communications* **15**, 3749 (2024).

40. Nelson, D. E., Randle, S. J. & Laman, H. Beyond ubiquitination: the atypical functions of Fbxo7 and other F-box proteins. *Open Biology* **3**, (2013).

41. Harris, R. *et al.* Fbxo7 promotes Cdk6 activity to inhibit PFKP and glycolysis in T cells. *Journal of Cell Biology* **221**, (2022).

42. UniProt: the Universal Protein Knowledgebase in 2023. *Nucleic Acids Res* **51**, 523–531 (2023).

43. Yu, G., Wang, L.-G., Han, Y. & He, Q.-Y. clusterProfiler: an R Package for Comparing Biological Themes Among Gene Clusters. *OMICS: A Journal of Integrative Biology* **16**, 284–287 (2012).

44. Roberts, D. J. & Miyamoto, S. Hexokinase II integrates energy metabolism and cellular protection: Akting on mitochondria and TORCing to autophagy. *Cell Death & Differentiation* **22**, 248–257 (2015).

45. Varanasi, S. K., Jaggi, U., Hay, N. & Rouse, B. T. Hexokinase II may be dispensable for CD4 T cell responses against a virus infection. *PLOS ONE* **13**, (2018).

46. Gerriets, V. A. *et al.* Metabolic programming and PDHK1 control CD4+ T cell subsets and inflammation. *The Journal of Clinical Investigation* **125**, 194–207 (2015).

47. Shi, L. Z. *et al.* HIF1α–dependent glycolytic pathway orchestrates a metabolic checkpoint for the differentiation of TH17 and Treg cells. *Journal of Experimental Medicine* **208**, 1367–1376 (2011).

48. Man, K. *et al.* The transcription factor IRF4 is essential for TCR affinity–mediated metabolic programming and clonal expansion of T cells. *Nature Immunology* **14**, 1155–1165 (2013).

49. Schmidt, C. *et al.* IRF4 is required for migration of CD4+ T cells to the intestine but not for Th2 and Th17 cell maintenance. *Frontiers in Immunology* **14**, (2023).

50. Mahnke, J. *et al.* Interferon Regulatory Factor 4 controls TH1 cell effector function and metabolism. *Scientific Reports* **6**, 35521 (2016).

51. Huber, M. & Lohoff, M. IRF4 at the crossroads of effector T-cell fate decision. *European Journal of Immunology* **44**, 1886–1895 (2014).

52. Lochner, M., Berod, L. & Sparwasser, T. Fatty acid metabolism in the regulation of T cell function. *Trends Immunol* **36**, 81–91 (2015).

53. Mashima, T., Seimiya, H. & Tsuruo, T. De novo fatty-acid synthesis and related pathways as molecular targets for cancer therapy. *British Journal of Cancer* **100**, 1369–1372 (2009).

54. Osinalde, N. *et al.* Nuclear Phosphoproteomic Screen Uncovers ACLY as Mediator of IL-2-induced Proliferation of CD4+ T lymphocytes*. *Molecular & Cellular Proteomics* **15**, 2076–2092 (2016).

55. Goldstein, J. L. & Brown, M. S. Regulation of the mevalonate pathway. *Nature* **343**, 425–430 (1990).

56. Mullen, P. J., Yu, R., Longo, J., Archer, M. C. & Penn, L. Z. The interplay between cell signalling and the mevalonate pathway in cancer. *Nature Reviews Cancer* **16**, 718–731 (2016).

57. Guerra, B. *et al.* The Mevalonate Pathway, a Metabolic Target in Cancer Therapy. *Frontiers in Oncology* **11**, (2021).

58. Cerqueira, N. M. F. S. A. *et al.* Cholesterol Biosynthesis: A Mechanistic Overview. *Biochemistry* **55**, 5483–5506 (2016).

59. Stefely, J. A. & Pagliarini, D. J. Biochemistry of Mitochondrial Coenzyme Q Biosynthesis. *Trends in Biochemical Sciences* **42**, 824–843 (2017).

60. Wilson, M. P. *et al.* A pseudoautosomal glycosylation disorder prompts the revision of dolichol biosynthesis. *Cell* **187**, 3585–3601 (2024).

61. Manaswiyoungkul, P., de Araujo, E. D. & Gunning, P. T. Targeting prenylation inhibition through the mevalonate pathway. *RSC Medicinal Chemistry* **11**, 51–71 (2020).

62. Gruenbacher, G. & Thurnher, M. Mevalonate Metabolism in Immuno-Oncology. *Frontiers in Immunology* **8**, (2017).

63. Gruenbacher, G. & Thurnher, M. Mevalonate metabolism governs cancer immune surveillance. *OncoImmunology* **6**, (2017).

64. Robinson, G. A., Waddington, K. E., Pineda-Torra, I. & Jury, E. C. Transcriptional Regulation of T-Cell Lipid Metabolism: Implications for Plasma Membrane Lipid Rafts and T-Cell Function. *Frontiers in Immunology* **8**, (2017).

65. Bietz, A., Zhu, H., Xue, M. & Xu, C. Cholesterol Metabolism in T Cells. *Frontiers in Immunology* **8**, (2017).

66. Aguilar-Ballester, M., Herrero-Cervera, A., Vinué, Á., Martínez-Hervás, S. & González-Navarro, H. Impact of Cholesterol Metabolism in Immune Cell Function and Atherosclerosis. *Nutrients* **12**, (2020).

67. Janesick, A. *et al.* High resolution mapping of the tumor microenvironment using integrated single-cell, spatial and in situ analysis. *Nature Communications* **14**, 8353 (2023).

68. O'Neill, L. A. J., Kishton, R. J. & Rathmell, J. A guide to immunometabolism for immunologists. *Nat Rev Immunol* **16**, 553–565 (2016).

69. Loftus, R. M. & Finlay, D. K. Immunometabolism: Cellular Metabolism Turns Immune Regulator. *Journal of Biological Chemistry* **291**, 1–10 (2016).

70. Lim, S. A., Su, W., Chapman, N. M. & Chi, H. Lipid metabolism in T cell signaling and function. *Nat Chem Biol* **18**, 470–481 (2022).

71. Raud, B., McGuire, P. J., Jones, R. G., Sparwasser, T. & Berod, L. Fatty acid metabolism in CD8+ T cell memory: Challenging current concepts. *Immunological Reviews* **283**, 213–231 (2018).

72. Sheppard, S. *et al.* Fatty acid oxidation fuels natural killer cell responses against infection and cancer. *Proceedings of the National Academy of Sciences* **121**, (2024).

73. Schimmer, S. *et al.* Fatty acids are crucial to fuel NK cells upon acute retrovirus infection. *Frontiers in Immunology* **14**, (2023).

74. Pacella, I. *et al.* Fatty acid metabolism complements glycolysis in the selective regulatory T cell expansion during tumor growth. *Proceedings of the National Academy of Sciences* **115**, 6546–6555 (2018).

75. Field, C. S. *et al.* Mitochondrial Integrity Regulated by Lipid Metabolism Is a Cell-Intrinsic Checkpoint for Treg Suppressive Function. *Cell Metabolism* **31**, 422–437 (2020).

76. Endo, Y., Kanno, T. & Nakajima, T. Fatty acid metabolism in T-cell function and differentiation. *Int Immunol* **34**, 579–587 (2022).

77. Tiwary, S., Berzofsky, J. A. & Terabe, M. Altered Lipid Tumor Environment and Its Potential Effects on NKT Cell Function in Tumor Immunity. *Frontiers in Immunology* **10**, (2019).

78. Koh, J. *et al.* De novo fatty-acid synthesis protects invariant NKT cells from cell death, thereby promoting their homeostasis and pathogenic roles in airway

hyperresponsiveness. *eLife* **12**, (2023).

79. Wakil, S. J. Fatty acid synthase, a proficient multifunctional enzyme. *Biochemistry* **28**, 4523–4530 (1989).

80. Lacher, S. M. *et al.* HMG-CoA reductase promotes protein prenylation and therefore is indispensible for T-cell survival. *Cell Death Dis* **8**, (2017).

81. Blank, N. *et al.* Atorvastatin Inhibits T Cell Activation through 3-Hydroxy-3-Methylglutaryl Coenzyme A Reductase without Decreasing Cholesterol Synthesis1. *The Journal of Immunology* **179**, 3613–3621 (2007).

82. Poggi, A., Boero, S., Musso, A. & Zocchi, M. R. Selective Role of Mevalonate Pathway in Regulating Perforin but Not FasL and TNFalpha Release in Human Natural Killer Cells. *PLOS ONE* **8**, (2013).

83. Mueller, A. & Strange, P. G. The chemokine receptor, CCR5. *The International Journal of Biochemistry & Cell Biology* **36**, 35–38 (2004).

84. Khan, I. A. *et al.* CCR5 Is Essential for NK Cell Trafficking and Host Survival following Toxoplasma gondii Infection. *PLOS Pathogens* **2**, (2006).

85. Ajuebor, M. N. *et al.* Lack of Chemokine Receptor CCR5 Promotes Murine Fulminant Liver Failure by Preventing the Apoptosis of Activated CD1d-Restricted NKT Cells1. *The Journal of Immunology* **174**, 8027–8037 (2005).

86. Xu, K. *et al.* Glycolysis fuels phosphoinositide 3-kinase signaling to bolster T cell immunity. *Science* **371**, 405–410 (2021).

87. Chen, X., Liu, L., Kang, S., Gnanaprakasam, J. N. R. & Wang, R. The lactate dehydrogenase (LDH) isoenzyme spectrum enables optimally controlling T cell glycolysis and differentiation. *Science Advances* **9**, (2025).

88. Finlay, D. K. Regulation of glucose metabolism in T cells: new insight into the role of Phosphoinositide 3-kinases. *Frontiers in Immunology* **3**, (2012).

89. Shyer, J. A., Flavell, R. A. & Bailis, W. Metabolic signaling in T cells. *Cell Research* **30**, 649–659 (2020).

90. Kim, E. H. & Suresh, M. Role of PI3K/Akt signaling in memory CD8 T cell differentiation. *Frontiers in Immunology* **4**, (2013).

91. Sauer, S. *et al.* T cell receptor signaling controls Foxp3 expression via PI3K, Akt, and mTOR. *Proceedings of the National Academy of Sciences* **105**, 7797–7802 (2008).

92. Soond, D. R., Slack, E. C., Garden, O. A., Patton, D. T. & Okkenhaug, K. Does the PI3K pathway promote or antagonize regulatory T cell development and function? *Frontiers in Immunology* **3**, (2012).

93. Handi, J., Patterson, S. J. & Levings, M. The Role of the PI3K Signaling Pathway in CD4+ T Cell Differentiation and Function. *Frontiers in Immunology* **3**, (2012).

94. Chellappa, S. *et al.* The PI3K p110δ Isoform Inhibitor Idelalisib Preferentially Inhibits Human Regulatory T Cell Function. *The Journal of Immunology* **202**, 1397–1405 (2019).

95. Johansen, K. H., Golec, D. P., Thomsen, J. H., Schwartzberg, P. L. & Okkenhaug, K. PI3K in T Cell Adhesion and Trafficking. *Frontiers in Immunology* **12**, (2021).

96. Abdullah, L., Hills, L. B., Winter, E. B. & Huang, Y. H. Diverse Roles of Akt in T cells. *Immunometabolism* **3**, (2021).

97. Glaviano, A. *et al.* PI3K/AKT/mTOR signaling transduction pathway and targeted therapies in cancer. *Molecular Cancer* **22**, 138 (2023).

98. Porstmann, T. *et al.* SREBP Activity Is Regulated by mTORC1 and Contributes to Akt-Dependent Cell Growth. *Cell Metabolism* **8**, 224–236 (2008).

99. Li, L.-Y. *et al.* Interplay and cooperation between SREBF1 and master transcription factors regulate lipid metabolism and tumor-promoting pathways in squamous cancer. *Nature Communications* **12**, 4362 (2021).

100. Horton, J. D. *et al.* Combined analysis of oligonucleotide microarray data from transgenic and knockout mice identifies direct SREBP target genes. *Proceedings of the National Academy of Sciences* **100**, 12027–12032 (2003).

101. Howie, D., Ten Bokum, A., Necula, A. S., Cobbold, S. P. & Waldmann, H. The Role of Lipid Metabolism in T Lymphocyte Differentiation and Survival. *Frontiers in Immunology* **8**, (2018).

102. Ruiz, R. *et al.* Sterol Regulatory Element-binding Protein-1 (SREBP-1) Is Required to Regulate Glycogen Synthesis and Gluconeogenic Gene Expression in Mouse Liver. *Journal of Biological Chemistry* **289**, 5510–5517 (2014).

103. Toriyama, K. *et al.* T cell-specific deletion of Pgam1 reveals a critical role for glycolysis in T cell responses. *Communications Biology* **3**, 394 (2020).

104. Horton, J. D. *et al.* Combined analysis of oligonucleotide microarray data from transgenic and knockout mice identifies direct SREBP target genes. *Proceedings of the National Academy of Sciences* **100**, 12027–12032 (2003).

105. Howie, D., Ten Bokum, A., Necula, A. S., Cobbold, S. P. & Waldmann, H. The Role of Lipid Metabolism in T Lymphocyte Differentiation and Survival. *Front Immunol* **8**, (2018).

106. Ruiz, R. *et al.* Sterol Regulatory Element-binding Protein-1 (SREBP-1) Is Required to Regulate Glycogen Synthesis and Gluconeogenic Gene Expression in Mouse Liver. *Journal of Biological Chemistry* **289**, 5510–5517 (2014).

107. Toriyama, K. *et al.* T cell-specific deletion of Pgam1 reveals a critical role for glycolysis in T cell responses. *Communications Biology* **3**, 394 (2020).

108. Chen, Y., Zhang, J., Cui, W. & Silverstein, R. L. CD36, a signaling receptor and fatty acid transporter that regulates immune cell metabolism and fate. *Journal of Experimental Medicine* **219**, (2022).

109. Jin, R. *et al.* Role of FABP5 in T Cell Lipid Metabolism and Function in the Tumor Microenvironment. *Cancers* **15**, (2023).

110. Skowronek, P. *et al.* Rapid and In-Depth Coverage of the (Phospho-)Proteome With Deep Libraries and Optimal Window Design for dia-PASEF. *Molecular & Cellular Proteomics* **21**, (2022).

111. Ritchie, M. E. *et al.* limma powers differential expression analyses for RNA-sequencing and microarray studies. *Nucleic Acids Res* **43**, (2015).